Different Fuel-Adopted Combustion Syntheses of Nano-Structured NiCrFeO₄: A Highly Recyclable and Versatile Catalyst for Reduction of Nitroarenes at Room Temperature and Photocatalytic Degradation of Various Organic Dyes in Unitary and Ternary Solutions

Sumit Singh, Shikha Sharma, Ujwal Manhas, Irfan Qadir, Amit Kumar Atri, and Devinder Singh*

ACCESS | Metrics & More | Article Recommendations | Supporting Information

ABSTRACT: As industrialization progresses, there is a large release of hazardous pollutants into the environment. These pollutants, which contain nitro compounds and organic dyes, are extremely dangerous due to their toxic and carcinogenic nature. An efficient, environmentally benign, and economical catalyst to degrade environmental pollutants or convert them into useful products has been of sustained interest in recent years. In this context, we report a simple and inexpensive combustion fabrication of NiCrFeO₄ using different fuels such as glycine, polyvinyl alcohol (PVA), and urea, showing tremendous catalytic and photocatalytic functionalities. Rietveld refinement and X-ray diffraction studies confirmed the formation of single-phase ferrites, with crystallite sizes ranging from 3.9 to 43.31 nm. The values of optical band gap,

obtained from the diffused reflectance spectroscopy technique, lie in the visible region range (1.50−1.60 eV), and hence, all the synthesized ferrites can act as good photocatalysts in the presence of visible light. All the NCF nanocatalysts were utilized for the reduction of nitroarenes and photocatalytic degradation of various cationic (RhB and MB) and anionic (MO) dyes and their mixture. NCFP displayed excellent activity for the reduction and oxidation reactions owing to its large surface area and low optical band gap. Furthermore, the photo-oxidative degradation by NCFP was also enhanced due to its low recombination of charge carriers as confirmed by the photoluminescence (PL) spectroscopy. NCFP efficiently reduces nitrobenzene to aminobenzene with 95% yield using sodium borohydride as the reducing agent in methanol medium at RT in 10 min. The results of photocatalytic activity have shown that the degradation efficiency of NCFP follows the order RhB > MB > MO in their unitary solution. Furthermore, in the case of the mixture of dyes, NCFP showed enhanced photocatalytic degradation for cationic dyes (RhB and MB) compared to that of anionic dye (MO). From the performance point of view, this catalyst can be useful in industrial application because of its high stability, greater catalytic efficiency, and cost-effectiveness.
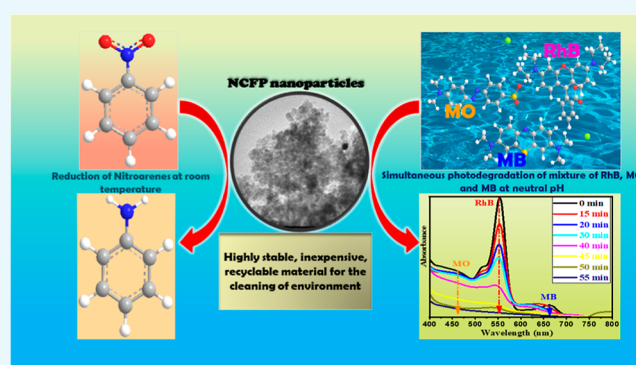
1. INTRODUCTION

In the past several years, magnetic nano-ferrites have been mostly investigated because of their enormous features, which are superior in contrast to their corresponding bulk counterparts,[1,2] like super-paramagnetism, high surface area, large surface to volume ratio, being smoothly separable under external magnetic field, and strong adsorption ability. One of the most interesting and important properties of nano-sized magnetic ferrites is catalysis, which is turning out to be a tactical field because it expresses a new route to face the challenges of energy and sustainability. Green and environment-friendly procedures of synthesis and conditions for reaction have played a crucial role toward the purpose of transforming hazardous processes to proficient ones. Such processes reduce the usage of harmful reagents and solvents,

hard reaction conditions, and also complex as well as time-consuming separation of catalysts from reaction mixtures.[3,4] Magnetic nano-ferrites have been proven to be in demand for carrying various tedious organic reactions.[5−7] By altering the size, chemical composition, morphology, or oxidation state of the metals used in the ferrite catalyst, enhancement and control over the reaction can be achieved by nano-catalysis.

Among the different heterogeneous catalysts, ferrites have been regarded as promising applicants for the efficient degradation/removal of a range of organic pollutants because of their extraordinary physical and chemical properties.[8,9] Additionally, ferrites possess high activity, good absorption of light, smooth transfer of mass, easy methodologies for preparation, and comfortable recyclability by applying an external magnet owing to their characteristic magnetic behavior.[10−12] The catalytic efficiency of spinel nano-ferrites strongly depends upon the method of preparation, annealing temperature, distribution of cations between tetrahedral and octahedral sites, and structural parameters like particle size, surface area, and presence of active surface sites. The redox potential and nature of the metal cation also have an influence on the catalytic performance of nano-ferrites.[13] A variety of expensive metal nanoparticles such as Au, Ag, Pt, Pd, metal oxides, and nanocomposites have been employed as catalysts, as they are very effective in removal or degradation of pollutants, but a green and inexpensive approach employing nano-ferrites as catalysts in such processes is facile and of wide applicability.[14−17] Various organic dyes and nitro compounds and their breakdown products have a carcinogenic effect on the humans as well as the biosphere.[18] So before discharging these dangerous pollutants in the environment, their removal or transformation into some useful products is very important for humans and environment. The transformation of toxic dyes into H_2O and CO_2 can be done by photocatalytic degradation. Reduction of carcinogenic nitroarenes to their corresponding amines is a useful conversion from the industrial and academic point of view, as the aromatic amines are starting materials for a number of biological and pharmaceutical compounds.[19] In the catalytic reduction of nitroarenes, reducing agents such as sodium borohydride and hydrazine hydrate have been recently used, but using sodium borohydride as a reducing agent has proven to be mild and safe without the formation of harmful byproducts.

$NiFe_2O_4$ has been found to be an excellent candidate in the treatment of organic pollutants. It is a soft magnetic material with an inverse spinel structure in which Ni^{2+} mostly reside at octahedral (B) and Fe^{3+} at tetrahedral [A] and octahedral (B) sites.[20] The distribution of metal cations among tetrahedral [A] and octahedral (B) sites greatly affects the structural, magnetic, and catalytic properties of ferrites,[21] as the catalytic activity mainly depends on the type of metal ion present at the catalytically active octahedral (B) site because octahedral sites of the ferrite sublattice are mainly exposed on the surface.[22] The chromium ion which has an antiferromagnetic nature affects the magnetic properties when introduced in the nickel ferrite lattice.[23] Ganure et. al.[24] reported a decrease in saturation magnetization in $NiFe_{2−x}Cr_xO_4$ (x = 0.1, 0.2, 0.3, and 0.4) as the Cr^{3+} ion concentration increases. The best catalytic activity was found with x = 0.4 for the synthesis of bis-(4-hydroxycoumarin) methane derivatives. Similarly, there is a linear decrease in the saturation magnetization with increase in chromium content in the nickel ferrite lattice as reported by Singhal and Chandra,[25] whereas coercivity increases slowly up to x = 0.8 but a large increase has been observed in samples x = 1 and 1.2. Ni- and Cu-doped nano-ferrites have been found to be excellent catalysts for the reduction of nitroarenes and photo-oxidative degradation of dyes. The $CuFe_2O_4$ nanoparticles showed tremendous catalytic performance with high recyclability using $NaBH_4$ as a reducing agent.[26,27] The catalytic activity of $CuFe_2O_4$ was enhanced using graphene as a support which was attributed to the synergistic effect of copper ferrite and graphene. The magnetically separable $NiFe_2O_4@Cu$ displayed excellent activity as a catalyst for reduction of nitroarenes to their corresponding amines. $NiFe_2O_4@Cu$ exhibited enhanced catalytic performance as compared to pure $NiFe_2O_4$ due to its larger surface area.[28] Cu/$SiO_2@NiFe_2O_4$, $SiO_2@NiFe_2O_4$, and $NiFe_2O_4$ nanocomposites were utilized as catalysts for reductive transformation of nitroarenes to amino arenes. A finely dispersed Cu ion in Cu/$SiO_2@NiFe_2O_4$ is responsible for its enhanced catalytic activity.[29] $Fe_{3−x}Cr_xO_4$ (x = 0.00, 0.18, 0.33, 0.47, and 0.67) was employed as a heterogeneous catalyst for Fenton-like degradation of organic dyes. It was observed that the surface area and degradation efficiency increase with the increment of the Cr^{3+}ion.[30] Ni^{2+}-doped $Ni_xCu_{1−x}Fe_2O_4$ (x = 0−0.5) displayed good photocatalytic activity for degradation of rhodamine-B (RhB), and it was found that x = 0.4 is the best among all the synthesized ferrites due to the high separation of electron and holes.[31] Sn(II) inserted on a hydroxyl apatite-encapsulated ($NiFe_2O_4@HAp-Sn^{2+}$) nanocatalyst and $NiFe_2O_4@SiO_2$ as a catalyst in the presence of H_2O_2 have also been found to be good candidates for the photo degradation of RhB.[32,33] Liu et. al.[34] reported oxalic acid-assisted photodegradation of RhB using $NiFe_2O_4$ where the complete degradation was achieved in 60 min. The photocatalytic degradation of the mixture of dyes has been carried out by a number of co-workers. $CoFe_2O_4$-reduced graphene oxide nanocomposites with different weight ratios were utilized for the photodegradation of various organic dyes and their mixture. The ratio 75CF-25RGO showed the highest photocatalytic performance toward the degradation of dyes and their mixture due to facile separation of charge carriers and synergistic effect of CF and RGO.[35] Photocatalytic degradation of various dyes and their mixture has also been reported by employing $ZnFe_2O_4/ZnO$ nanocomposites as photocatalysts. The enhanced degrading capability of a nanocomposite as compared to pristine $ZnFe_2O_4$ has been explained on the basis of suppression of recombination of photo-induced charge carriers.[36]

To the best of our knowledge, there is no report on the synthesis of nano-sized chromium-doped nickel ferrite $NiCrFeO_4$ via a combustion method using different fuels. In view of this, we report a facile and simple fabrication of chromium-doped nickel ferrite $NiCrFeO_4$ by a combustion method using different fuels such as glycine, urea, and polyvinyl alcohol (PVA). Moreover, we are reporting for the first time the catalytic activity of the $NiCrFeO_4$ for both reduction of nitroarenes and photo-oxidative degradation of organic dyes in their unitary as well as ternary solutions. Catalytic activity of the materials was studied for the reduction of nitroarenes to the corresponding amines because the aromatic amines are the starting materials for various biological and pharmaceutical active compounds. It is well known that there are many kinds of organic dyes in industrial wastewater, and they may cause long-term ill effects on environment and human health. In real practice, it is common to find wastewater that contains more than one kind of dyes. It is hence meaningful to investigate the photocatalytic efficiency of prepared nano-catalysts in the treatment of wastewater that contains different dyes. Therefore, in the present study, RhB dye was chosen as a model pollutant, and under the same conditions, methylene blue (MB), methyl orange (MO), and their mixture were targeted and degraded. Hence, the present work aims to study the comparative effect of prepared ferrites

Scheme 1. General Scheme for the Synthesis of NCFG, NCFP, and NCFU Nanocatalysts
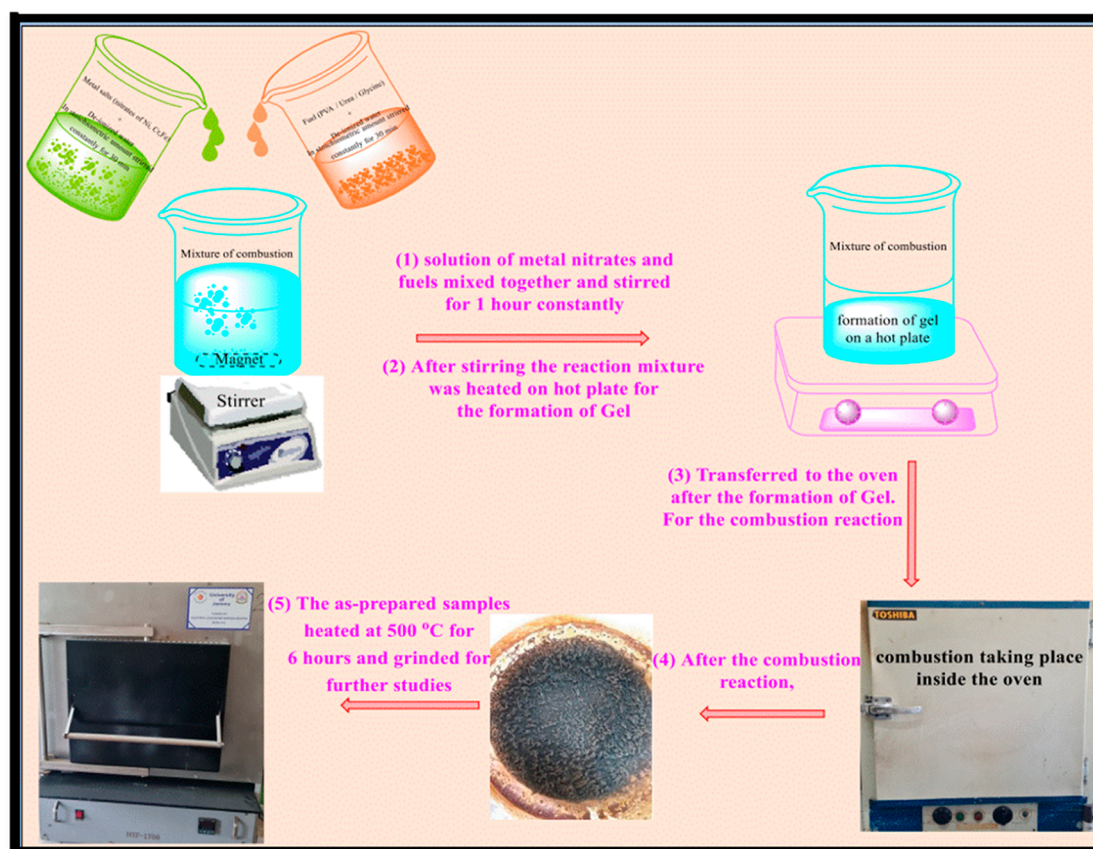
on the photo-oxidative degradation of dyes and reduction of nitroarenes to amines. The comparative catalytic efficiency of the prepared ferrites was investigated based on the surface area, photoluminescence (PL) spectroscopy, and optical band gap. The simple method of preparation and multifunctional character of a NiCrFeO$_4$ nanocatalyst makes it a versatile catalyst in the field of reduction of nitroarenes and photocatalysis, which can be useful for treating environmental issues.

2. EXPERIMENTAL SECTION

2.1. Materials and Reagents. The materials and reagents used are ferric nitrate nonahydrate (Fe(NO$_3$)$_3$·9H$_2$O), nickel nitrate hexahydrate (Ni(NO$_3$)$_2$·6H$_2$O), chromium nitrate nonahydrate (Cr(NO$_3$)$_3$·9H$_2$O), glycine (NH$_2$CH$_2$COOH), urea (NH$_2$CONH$_2$), PVA (C$_2$H$_4$O), sodium borohydride (NaBH$_4$), methanol (CH$_3$OH), RhB (C$_{28}$H$_{31}$N$_2$O$_3$Cl), MB (C$_{16}$H$_{18}$ClN$_3$S), MO (C$_{14}$H$_{14}$N$_3$NaO$_3$S), and hydrogen peroxide (H$_2$O$_2$, 27% w/w). All the chemicals used in the reactions were purchased from the Alfa Aesar and were of analytical grade and utilized as obtained without any further purification.

2.2. Fabrication of Nickel Chromium Ferrite Nanoparticles. In the present work, nickel chromium ferrite nanoparticles were fabricated by the solution combustion method which is preferred for its simplicity, short time requirement for reaction, and low calcination temperature. These features have enabled ferrite nanoparticles to have a fine particle size, diminished impurities, and enhanced physical properties.[37,38] In this method, the metal nitrates were used as an oxidant and source of required cations. Fuel is generally a

source of carbon and hydrogen, yielding gaseous products like CO$_2$ and H$_2$O. In addition to this, fuel also works as a complexing agent providing a homogenous distribution of metal cations in the solution. The stoichiometry of the mixture of metal nitrates and different fuels was calculated based on the total oxidizing and reducing valencies of oxidizer (O), that is, metal nitrates and fuel (F), respectively, so that the value of equivalence ratio that Φ_e (O/F) becomes unity and maximum heat is evolved.[39] Therefore, in order to synthesize NiCrFeO$_4$, the various reactants were taken in molar proportion 1:1:1:x of Ni(NO$_3$)$_2$, Fe(NO$_3$)$_3$, Cr(NO$_3$)$_3$, and fuel where x = 4.44, 6.66, and 4 for glycine, urea, and PVA, respectively. The solutions of weighed metal nitrates and fuel were individually stirred constantly for about 30 min by utilizing a magnetic stirrer, and then both the solutions transferred into the beaker and stirred for 60 min to form homogenous solution for combustion. The well-stirred homogenous solution was then put on a hot plate and heated at a temperature of about 100−120 °C to form a gel. The gel was further heated in an oven at 250 °C for combustion reaction, which yields a voluminous and fluffy mass in the beaker. The as-prepared ferrites were annealed in a muffle furnace at 500 °C for 6 h, and finally the annealed ferrites were grounded to fine powder in the agate mortar and pestle. The powders were named as NCFG, NCFU, and NCFP, respectively, for the nanoparticles synthesized by using glycine, urea, and PVA as a fuel. Scheme 1 shows the schematic diagram for the synthesis of the NCFG, NCFP, and NCFU nanoparticles.

2.3. Physical Measurements. The thermal analysis of the prepared nano-catalysts was conducted on PerkinElmer
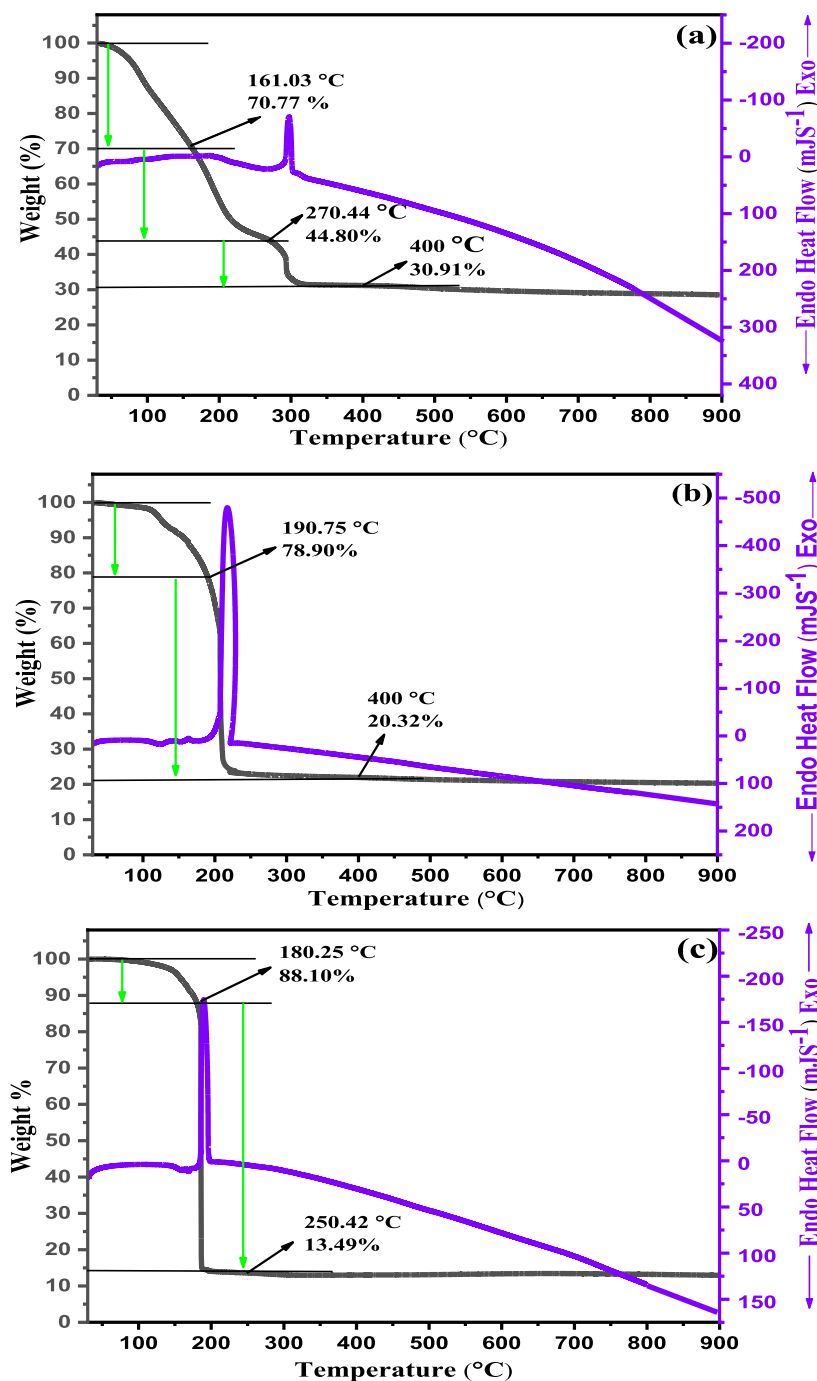
Figure 1. TGA and DTA curves for (a) NCFP, (b) NCFU, and (C) NCFG nanocatalysts.

thermal analyzer (STA-6000). For the structural characterization of the prepared samples, powder X-ray diffraction (XRD) was done on an X-ray diffractometer (Rigaku Smart Lab 9 kW rotating X-ray diffractometer) in the 2θ range of $10-100°$. High-resolution transmission electron microscopy (HRTEM) for determining the particle size was performed using Technai G2 20. For the morphology and elemental analysis, field emission scanning electron microscopy (FESEM) and energy-dispersive X-ray (EDX) were performed using Zeiss GeminiSEM. For the purpose of specific surface area, the N_2 adsorption method was used by employing the BET (BELSORP MINIX) instrument after preheating the samples at 100 °C for 5 h. The PL emission spectra were

recorded at room temperature by utilizing a fluorescence spectrophotometer (Hitachi, F-4700) equipped with a xenon lamp as a source of excitation. To determine the magnetic behavior of the samples room temperature, M versus H curves were recorded using a vibrating sample magnetometer (Lake Shore 7410-series VSM). For the determination of the optical band gap of the nano-ferrites, diffused reflectance spectroscopy (DRS) spectra and the time-dependent spectra of degradation of different dyes were taken by UV−visible spectroscopy by utilizing a UV−vis−NIR spectrophotometer (PerkinElmer, model LAMBDA 1050$^+$). ^{1}HNMR (400 MHz) and ^{13}CNMR (100 MHz) were recorded in CDCl$_3$, MeOD, and DMSO on a Bruker Advance III spectrometer using TMS as a standard.

2.4. Catalytic Activity Measurement. In order to demonstrate the capability of the prepared NCF nanoparticles as heterogeneous catalysts, the catalytic performance of all the prepared nano-ferrites was studied for both photo-oxidation and reduction reactions. By keeping the environmental issues in mind, the reduction and photo degradation of toxic, carcinogenic, hazardous nitroarenes, and organic dyes have been taken as model reactions.

2.4.1. Procedure for the Catalytic Reduction of Nitro-arenes. A solution containing nitroarene (1 mmol) in methanol (5 mL) was prepared in a round bottom flask (50 mL). To the abovementioned solution, a catalyst 0.05 mmol (12 mg) was added, and the mixture was then stirred for 2 min. Thereafter, $NaBH_4$ (8 mmol) was added to the reaction mixture when a vigorous reaction took place. The reaction mixture was continued to be stirred at room temperature and the reaction progress was checked by TLC (eluent; EtOAc/hexane: 3:10). After the completion of reaction, the reaction mixture was supplied with 5 mL of deionized water and again stirred for 10 min. Then, the mixture was extracted with ethyl acetate (3 × 10 mL) followed by drying over anhydrous sodium sulphate. The crude product was obtained and dried after evaporating the solvent. Furthermore, the crude product was purified by using column chromatography over silica gel 100−200 mesh size (eluent; EtOAc/hexane: 3:10) to yield the pure amino arenes. Elucidation of structures of the obtained product was confirmed by ^{1}HNMR and ^{13}CNMR. To check the recyclability of the ferrites, the separated catalyst was then washed with de-ionized water and ethanol several times to withdraw any organic and inorganic impurities and finally dried in an oven.

2.4.2. Photo-Oxidative Degradation of Organic Dyes and Their Mixtures. Various organic dyes were chosen for the photo-oxidative degradation which was performed under visible light irradiation (250 W mercury vapor lamp), and the distance between the light source and the dye solution was 15 cm. For typical photo-oxidative reaction, aqueous solution of different dyes like RhB, MB, and MO (15 mg/L) was prepared in de-ionized water and 100 mg of the catalyst was added in 100 mL of aqueous solution of dye in a 400 ml beaker. For degradation of a mixture of MO, MB, and RhB, 100 mL solution was taken containing equal volume of each dye. To achieve the adsorption−desorption equilibrium, the reaction solution was stirred in dark for about 1 h. Before exposing the solution to the visible light, 1 mL of H_2O_2 was added and stirring was continued thereafter. The sample solution (3 mL) was withdrawn at set time intervals and immediately centrifuged for regular time intervals to remove the catalyst completely, and any changes in the dye concentration was examined by a UV−visible spectrophotometer. At the end of the degradation reaction, the catalyst was washed 3−4 times with ethanol and water and dried in an oven for further use in recycling reactions to check the recyclability and stability of the catalyst.

3. RESULTS AND DISCUSSION

3.1. Thermogravimetric and Differential Thermal Analysis. Thermogravimetric analysis (TGA) and differential thermal analysis (DTA) of NCFG, NCFP, and NCFU catalysts were carried out in order to study their thermal stability. The experiments were done under a N_2 atmosphere with the heating rate of 10 °C/min, and the corresponding TGA and DTA curves are shown in Figure 1. From Figure 1a, it can be
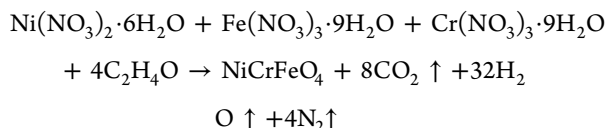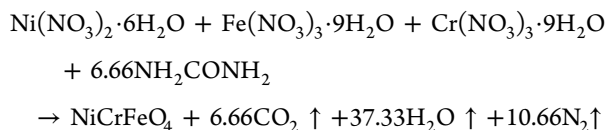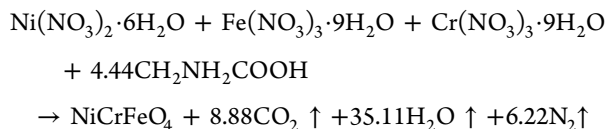
clearly seen that the thermal decomposition of the NCFP precursor gel takes place in three steps, while one endothermic and two exothermic peaks are shown by the DTA curve. The first step of decomposition occurs in the temperature range of 30−160 °C, in which 30% of weight is lost, while no significant peak is present in the DTA curve for this range. This weight loss may be due to the decomposition of hydroxyl groups of PVA and weakly attached water. The second step occurred as shown in the TGA curve within the temperature range of 160−270 °C with weight loss of almost 25%, accompanied by a small endothermic at 270 °C and an exothermic peak at the temperature 190 °C in DTA. This may be due to the loss of organic impurities and start of redox reaction between the metal nitrates and the fuel PVA. In the third step, combustion reaction between the metal nitrates (carrying oxidizing valency) and PVA (carrying reducing valency) takes place in the temperature range of 270−400 °C with an exothermic peak at 300 °C, while weight loss in this step is about 15%. Above 400 °C, the weight loss is quite negligible showing that the major weight loss occurs below 400 °C and a total of 70% weight is lost during the combustion reaction in the case of PVA.

The TGA curve for precursor gel NCFU (Figure 1b) shows the two steps of weight loss which is accompanied by one endothermic and two exothermic peaks in the DTA curve. The total loss of weight is about 80% up to 400 °C. Weight loss in the first stage occurs in the temperature range 30−190 °C with one endothermic peak around 125 °C and one exothermic peak around 163 °C, which may be due to the complete evaporation of water molecules and start of combustion reaction between the metal nitrates and urea fuel. About 22% of weight is lost during the first stage of decomposition. As shown in Figure 1b, the second stage of weight loss occurs in the temperature range of 190−400 °C accompanied by a strong exothermic peak around 220 °C, which corresponds to the decomposition of reactant molecules and occurrence of combustion reaction between metal nitrates and urea with the evolution of water, CO_2, ammonia, N_2, and oxides of nitrogen, while the residual organic impurities decompose at a temperature around 400 °C.[40,41] Weight loss associated with this stage is about 58%. Above the temperature of 400 °C, the weight remains almost constant, implying the formation of the desired crystalline phase.

The thermal decomposition of precursor gel NCFG (Figure 1c) is taking place in two steps along with one endothermic and one exothermic peak in the DTA curve. Weight loss in the first step corresponds to the temperature range of 30−180 °C with one endothermic peak in DTA around 170 °C. The 12% weight loss in this step can be due to the evaporation of water, organic impurities, and start of a combustion reaction between the metal nitrates and glycine. The second step of weight loss occurs in temperature range of 180−250 °C along with an exothermic peak in the DTA at 190 °C. The percent of weight loss associated with this exothermic peak is 75%, which may be due to occurrence of combustion reaction because of interaction of glycine and metal nitrates in the gel with the evolution of water, CO_2 and N_2. The total weight loss in the decomposition process is about 87% and no significant weight loss can be seen above the temperature 210 °C, that is, weight after 210 °C remains almost constant, a clear indication of the formation of a crystalline spinel structure. Thus, it can be seen from thermal treatment that decomposition of a precursor gel of sample NCFP starts first, then decomposition of a precursor

gel of sample NCFU occurs, and finally, the decomposition of precursor gel of sample NCFG occurs.

The possible reactions taking place during combustion of different fuels with metal nitrates are as follows

$$Ni(NO_3)_2\cdot 6H_2O + Fe(NO_3)_3\cdot 9H_2O + Cr(NO_3)_3\cdot 9H_2O$$
$$+ 4.44CH_2NH_2COOH$$
$$\rightarrow NiCrFeO_4 + 8.88CO_2 \uparrow + 35.11H_2O \uparrow + 6.22N_2\uparrow$$

$$Ni(NO_3)_2\cdot 6H_2O + Fe(NO_3)_3\cdot 9H_2O + Cr(NO_3)_3\cdot 9H_2O$$
$$+ 6.66NH_2CONH_2$$
$$\rightarrow NiCrFeO_4 + 6.66CO_2 \uparrow + 37.33H_2O \uparrow + 10.66N_2\uparrow$$

$$Ni(NO_3)_2\cdot 6H_2O + Fe(NO_3)_3\cdot 9H_2O + Cr(NO_3)_3\cdot 9H_2O$$
$$+ 4C_2H_4O \rightarrow NiCrFeO_4 + 8CO_2 \uparrow + 32H_2$$
$$O \uparrow + 4N_2\uparrow$$

3.2. Phase and Structural Determination: XRD and Rietveld Refinement. In order to determine the effect of fuels used on the crystal structure of the samples, XRD analysis was performed on each sample after heat treatment. Figure S1 shows typical X-ray diffractograms of NiCrFeO$_4$ ferrites synthesized using glycine, urea, and PVA as fuels. The diffraction maxima corresponding to the reflection planes (111), (220), (311), (222), (400), (422), (511), and (440) with no characteristic impurity peaks were observed which correspond to spinel cubic structure with the $Fd\bar{3}m$ space group. Moreover, the Rietveld refinement was done on XRD data to obtain complete information regarding the crystal structure of the samples prepared using different fuels using GSAS/EXPGUI program[42,43] by implementing significant structural information from the literature in the space group $Fd\bar{3}m$. Figure 2 displays the plots of Rietveld refinement for the synthesized samples. It can be seen that the observed and calculated diffraction patterns are in good agreement which is confirmed by the linearity of difference in measured and calculated XRD patterns. The various Rietveld refined structural parameters for the samples like goodness of fit (χ^2), reliability factors (R_{wp} and R_p), and oxygen positional parameter (O) are given in Table 1. The values of χ^2 are reliable to assign crystal structure to the prepared phases without any impurity. XRD data further allow us to examine the effect of different fuels on structural parameters such as crystallite size (D) and lattice constant (a) for the NCF nanoparticles. The values of the lattice constant obtained from Rietveld refinement for the samples NCFG, NCFU, and NCFP are tabulated in Table 1. The variation in the values of the lattice constant may be justified on the basis of the fact that the different fuels lead to the formation of phases having different cationic distribution between tetrahedral and octahedral sites of the spinel structure and hence the volume (V) of the prepared samples changed according to values of lattice constant, as given in Table 1. By applying the classical Debye–Scherrer equation, the crystallite size of prepared samples was calculated from the line broadening of the most intense (311) peak[44]

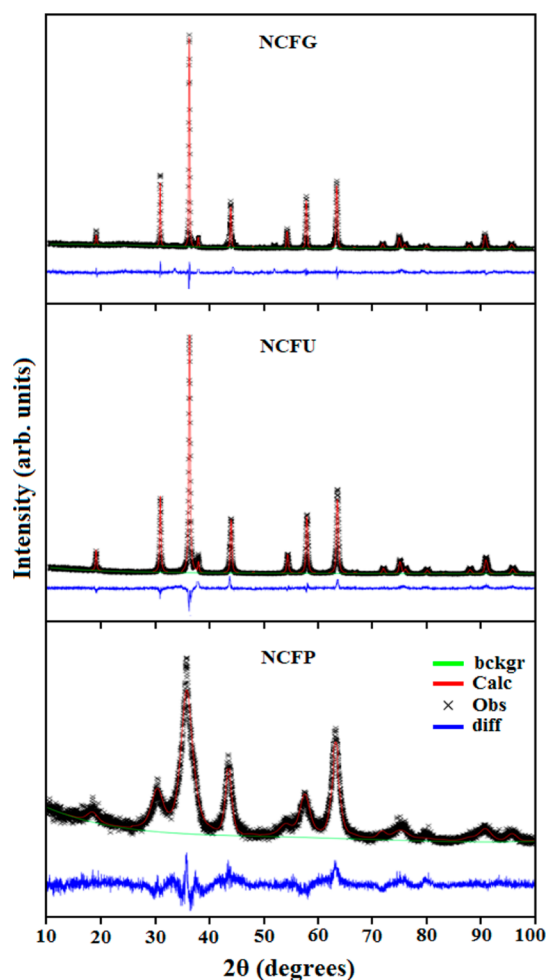$$D = \frac{0.9\lambda}{\beta \cos \theta} \qquad (1)$$

Figure 2. Rietveld refinement plots of NCF nanocatalysts.

Table 1. Structural Parameters Obtained from the Rietveld Refinement of the XRD Pattern for NiFeCrO$_4$ Samples Calcined at 500 °C[a]

sample	NCFG	NCFP	NCFU
a (Å)	8.2879(2)	8.3072(9)	8.3022(1)
O	0.2526(5)	0.2520(5)	0.2536(2)
V (Å³)	569.29(2)	573.28(11)	572.24(1)
D (nm)	43.31	3.90	30.13
R_{wp}	0.2391	0.1444	0.1711
R_p	0.1628	0.1095	0.1147
χ^2	3.802	1.590	2.106

[a]The atomic sites are: Ni/Fe 8a [0.125, 0.125, 0.125]; Ni/Fe/Cr 16d [0.5, 0.5, 0.5]; O 32e in the space group $Fd\bar{3}m$.
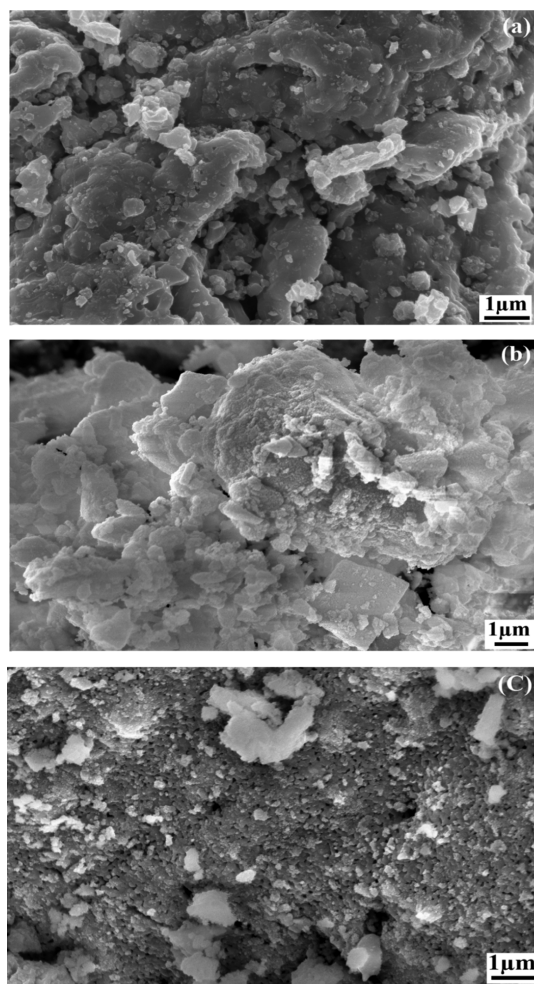
where D is the crystallite size of nanoparticles, λ denotes the wavelength of radiation used (1.54 Å), θ is the angle of diffraction, and β is full width at half maxima. Since the Braggs peak width is an integration of sample and instrument-dependent effects, thus the value of β can be calculated using the following formula[45]

$$\beta = \sqrt{[(\beta^2_{measured}) - (\beta^2_{instrumental})]} \qquad (2)$$

The values of crystallite size calculated using eq 1 are summarized in Table 1. It can be depicted from Table 1 that the crystallite size is dependent on the nature of fuel used. The difference in crystallite size can be credited to the different
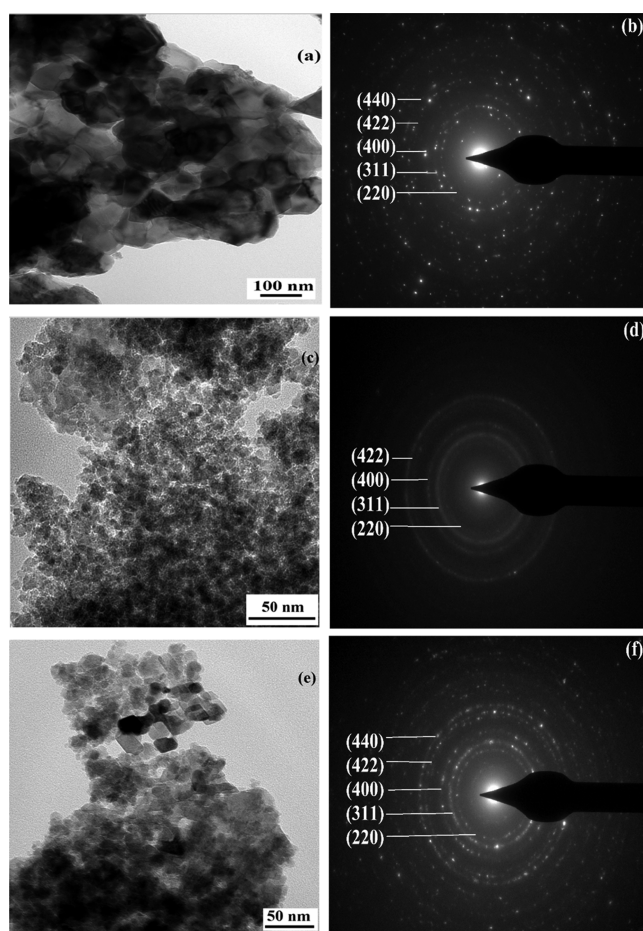
decomposition temperature of fuels. It is well known that the greater the decomposition temperature of fuel, the higher will be the nucleation and growth of the particles, and therefore the larger is the crystallite size and vice versa.[46]

3.3. Morphology, Shape, and Purity of the Nano-catalysts.

To examine the role of different fuels on the morphology, particle size, and crystallinity of the prepared samples, FESEM and HRTEM studies were conducted. The typical FESEM micrographs of the NCFG, NCFP, and NCFU are given in Figure 3. The FESEM images show the presence of

Figure 4. High-resolution TEM images and SAED patterns of NCFG (a,b), NCFP (c,d), and NCFU (e,f).

Figure 3. FESEM micrographs for (a) NCFG, (b) NCFP, and (c) NCFU.

small voids and pores in all the samples. This may be attributed to the release of a large number of gases like carbon dioxide, water, and nitrogen during the combustion reaction. The NCFG sample has a sponge-like structure with high agglomeration, which consists of very fine crystallites. A dense microstructure for NCFU has been observed with little pores on the surface. Moreover, all the crystallites are connected very well with each other, which may be attributed to the crystalline formation of phase. A porous-like structure of sample NCFP was observed with irregular shape and such porous morphology can offer a high surface area. For the purpose of HRTEM, all the nanocatalysts were dispersed in ethanol and sonicated for 1 h to get the clear dispersion. The HRTEM images (Figure 4) clearly displayed the spherical shape of the particles with visible boundaries. The average

particle size for NCFP obtained from HRTEM is of the order of 5.5 and 35.4 nm for NCFU and 80.2 for NCFG nanoparticles. The variation in the particle size could be due to the difference in decomposition temperature of the fuels. In the case of NCFP, the particle size is 5.5 nm, which is slightly bigger than the crystallite size (3.9 nm), clearly indicating that the extent of agglomeration is quite low. The NCFG particle size is almost double the crystallite size, indicating that the growth of the particle is quite good. Selected area electron diffraction (SAED) patterns (Figure 4) display high crystallinity with a set of strong diffraction rings, which are well aligned with the XRD peaks. The major peaks in the XRD were also seen in the SAED pattern's diffraction rings (220), (311), (400), (422), and (440), as shown in Figure 4b,d,f. The elemental composition was detected using the EDX technique for all the samples. All the peaks in the EDX spectra are Ni, Fe, Cr, and O with no extra peak of any other element. The typical EDX spectra are shown in Figure S2.

3.4. BET Surface Area.

To study the impact of fuel on morphologies obtained over the specific surface area of samples having the same composition is quite very interesting. It is reported in the literature that the more the specific surface area, the more would be its catalytic efficiency.[47] Thus, the information regarding the specific surface area, appearance, that is, meso/macro or microporous and nature of the nanoscale pores is necessary in defining the surface-dependent properties of the nanoscale ferrite materials. Therefore, to determine the detailed role that the surface area plays in all the

samples in the catalytic activity, the technique coined by Brunauer, Emmett, and Teller, mostly known as the BET surface area analysis, was utilized. For the analysis, all the samples NCFG, NCFP, and NCFU were preheated at 100 °C for 5 h before N_2 adsorption. The adsorption/desorption isotherms of N_2 for the nano-ferrites are displayed in Figure S3. The adsorption−desorption isotherms of N_2 at 77 K for NCFP and NCFU lead to the type IV isotherm hysteresis, demonstrating the mesoporous nature of both the samples, according to the classification of the IUPAC,[48] while no hysteresis was shown by the sample NCFG. The type IV shows the monolayer adsorption at low pressure and multilayer adsorption at high pressure.[49,50] The values of specific surface area, total pore volume, and mean pore diameter obtained from BET adsorption isotherm are given in Table 2. It can be

Table 2. Specific Surface Area, Total Pore Volume, and Mean Pore Diameter for NCFG, NCFU, and NCFP Nanoparticles

s. no.	sample	specific surface area (m²/g)	total pore volume (cm³/g)	mean pore diameter (nm)
01	NCFG	1.16	0.0004	1.4027
02	NCFP	90.6	0.1407	6.2118
03	NCFU	24.9	0.0761	12.251

concluded from Table 2 that the specific surface area among the three ferrite nanocatalysts follows the order NCFP > NCFU > NCFG. The largest surface area of NCFP could be due to its small crystallite and grain size as already confirmed by XRD and HR-TEM measurements. On the basis of mean pore diameter, all the ferrite nanoparticles may be classified as meso or micro pores, that is, NCFP and NCFU have the mean pore diameter in the range 2−50 nm and hence can be classified as mesopores,[51] whereas NCFG with the diameter <2 nm is classified as a micropore material.

3.5. Optical Properties. The optical band gap is a necessary factor for establishing the potential functions of a material as an efficient photocatalyst in the visible light. UV−vis DRS was employed because of its efficiency for examining the optical properties and predicting the band gap of a material. In spinel ferrites, the band structure suggests energy which is involved to excite an electron from the O 2p orbital, that is, valence band, to Fe 3d, that is, conduction band and the required energy for such an electronic transition is directly proportional to the band gap of ferrite material.[52] The inset of Figure 5 displays the DRS spectra taken in the range of 250−1100 nm at room temperature for the purpose of band gap determination.

The most widely used Kubelka−Munk theory is utilized to analyze the DRS spectra. The Kubelka−Munk function $F(R)$ is in direct proportion to the absorption coefficient as

$$(F(R)) \equiv \alpha = \frac{(1-R)^2}{2R} \qquad (3)$$

where $F(R)$ is the Kubelka−Munk function, α is the absorption coefficient, and R is the reflectance.

The correlation between E_g and α is called as the Tauc plot, in which E_g is the band gap of the nanoparticle.[53,54] Thus from eq 3, the Tauc relation becomes as follows

$$F(R)h\nu = A(h\nu - E_g)^n \qquad (4)$$
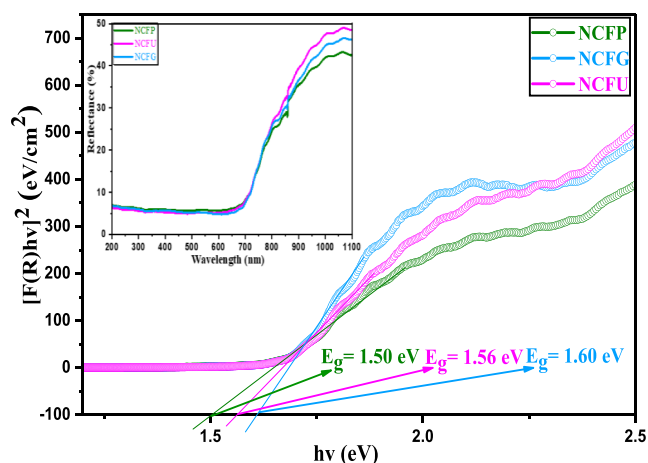
Figure 5. Tauc plot of $(F(R)h\nu)^2$ vs $h\nu$ of NCF nanocatalysts (inset shows the DRS spectra of NCF nanoparticles).

where h is the Planck's constant, ν is the photon energy frequency, A is the proportionality constant, and E_g is the optical band gap. Here, n is the nature of electronic transition occurring in the material. It has different theoretical values for different transitions, that is, 2 for indirect allowed and 1/2 for direct allowed transition. It is evident from the literature that spinel ferrites are a class of materials which have a direct band gap,[55] and hence, in the present case, the value of n is taken to be 1/2. A graph between $(F(R)h\nu)^2$ versus $h\nu$ (Figure 5) known as the Tauc plot is plotted, and the unique values of the band gap is calculated by extrapolating $(F(R)h\nu)^2 = 0$. The acquired values of band gap are tabulated in Table 3. It can be seen that there is a significant decrease in the band gap values from NCFG to NCFP. Generally, the band gap of a material is governed by two important factors: "quantum confinement effect" and "surface and inter-surface effects". The value of the band gap increases with decrease in crystallite size, obeying the quantum confinement effect, and a blue shift (increase) is observed, while inverse is the case in the surface and inter-surface effect, which induces a red shift (decrease) in the band gap with decreasing crystallite size.[56] The variation in the values of the band gap of our samples may be attributed to the dominance of the surface and inter-surface effect over the quantum confinement effect; thus, the band gap induces a red shift (decrease) with a decrease in the crystallite size as reported earlier.[57] Similar results of the band gap with a crystallite size can also be seen from the literature.[58−60] It is quite noticeable that the calculated values of the band gap of all the prepared nanosamples lie in the visible range, which is a clear indication that the samples can act as good photocatalysts in visible light.[61]

3.6. Magnetic Properties. It is quite interesting to view the impact of fuel on magnetic properties of the prepared nano-ferrites. To determine the magnetic behavior of all the $NiCrFeO_4$ nanoparticles, vibrating sample magnetometer (VSM) measurements with an applied magnetic field of ±20 kOe were done at room temperature. Typical room temperature hysteresis loops for the nano-ferrites synthesized by using different fuels are shown in Figure 6. It can be observed that magnetization of all the nano-ferrites does not show saturation in magnetization even at maximum applied magnetic field of ±20 kOe. Such non-saturating behavior displayed by the ferrite materials may be due to the presence of two characteristics: (i) antiferromagnetic and/or (ii) superparamagnetic, as suggested

Table 3. Values of Various Magnetic Parameters and Optical Band Gap of NCFP, NCFU, and NCFG

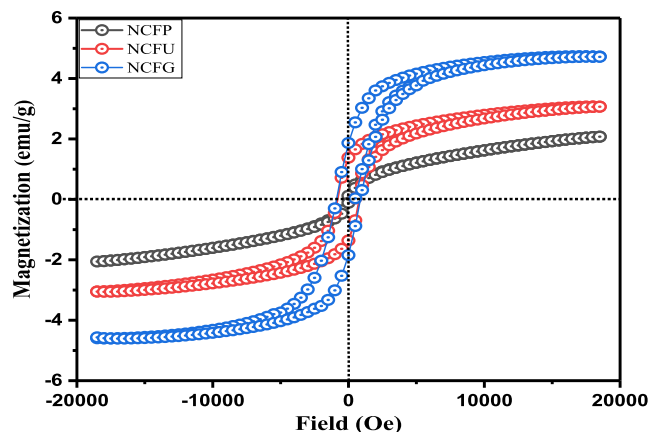| ferrite nanoparticles	saturation magnetization (M_s)(emu/g)	remanence (M_r) (emu/g)	coercivity (H_c) (Oe)	squareness ratio $(S = M_r/M_s)$	band gap (eV)	magnetic anisotropic constant K (erg/cm^3)
NCFG	5.02	0.91	376.5	0.180	1.60	1928.6
NCFP	2.69	0.11	108.6	0.004	1.50	298.1
NCFU	3.56	0.91	299.2	0.255	1.56	1086.9

Figure 6. Room temperature hysteresis loops for NCF nanocatalysts.

by Desai et al.[62] The magnetization M_s values were predicted from the plot between M_s and $1/H$ in the high field region. The different magnetic parameters like saturation magnetization (M_s), coercivity (H_c), remanence (M_r), and squareness ratio $(S = M_r/M_s)$ are summarized in Table 3. The difference in magnetic parameters is attributed to the nature of fuel used. It can be concluded from Table 3 that the maximum value of saturation magnetization (5.02 emu/g) is observed for the NCFG sample, while the NCFP sample shows a minimum value of 2.69 emu/g. It is well established that the particle size of ferrites has a significant effect on the saturation magnetization and coercivity, and the larger the particle size, the higher will be its saturation magnetization.[63] The bigger crystallite size and high crystallinity of NCFG in comparison to NCFU and NCFP samples as can be seen from the powder XRD data (Table 1) therefore leads to higher saturation magnetization of NCFG. The lower M_s value of small-sized NCFP nano-ferrite may be due to disordered spins that are present on the surface, which inhibits the core spin from aligning in the direction of the field.[64] An increase in the coercivity is found from NCFP to NCFU to NCFG, which follows the same trend as of saturation magnetization. This variation in coercivity is related to particle size. Such a variation in coercivity with particle size is clear evidence that particles are in a single domain region.[65,66] The increase in coercivity with particle size can also be explained by a magnetic anisotropic constant (K), that is, greater the value of K, larger is the coercivity. The value of K can be calculated by using relation[67]

$$K = \frac{M_S \times H_C}{0.98} \tag{5}$$

where K is the anisotropic constant, M_s is saturation magnetization, and H_c is coercivity. The calculated values of K are summarized in Table 3. The squareness ratio (S) is used to establish whether the inter grain exchange exists or not. Stoner and Wohlfarth have reported $S = 0.5$ for randomly oriented non-interacting particles, while $S < 0.5$ for particles

that interact by magnetostatic interactions.[68] In the present investigation, S is less than 0.5 for all the samples, indicating that interactions are magnetostatic. It is quite notable that the nanosized and single-domain ferromagnetic powder could be superparamagnetic with a squareness ratio $(S) = 0$.[69] In the present case, the small coercivity and almost zero squareness ratio value of NCFP depicts the superparamagnetic character of the sample due to its small particle size and uniform shape, which is in good conformity with the results published in the literature.[70,71]

3.7. Catalytic and Photocatalytic Properties. *3.7.1. Catalytic Reduction of Nitroarenes.* For the evaluation of catalytic activity of the prepared nanocatalysts, that is, NCFG, NCFP, and NCFU, reduction of nitrobenzene was chosen as model reaction using sodium borohydride as a reducing agent. Before optimizing the various reaction parameters, the control experiments were carried out, one in the presence of a catalyst and other in the absence of a catalyst. It was observed that reaction without a catalyst did not proceed at all, which indicates the necessity of a catalyst for the reduction to occur. Moreover, sodium borohydride itself cannot reduce the nitroarenes without any other additives.[72] To obtain the maximum yield of the desired product, optimization of the reduction reaction was performed with 1 mmol of nitrobenzene. Prior to the process of optimization, we investigated various conditions including type of solvent, the amount of catalyst, and amount of sodium borohydride.

3.7.1.1. Optimization of Various Reaction Components. Optimization of the type of solvent: primarily, the model reaction was examined in various solvents such as MeOH, EtOH, CH$_3$CN, CH$_3$CN/H$_2$O, H$_2$O/EtOH, and H$_2$O. Among them, MeOH yielded the best results. The effect of various solvents on the reduction of nitroarenes is given in Table 4.

Table 4. Effect of Different Solvents on the Reduction of Nitroarenes^a Catalyzed by the NCFP Nanocatalyst

s. no.	solvent	time (min)	yield^b (%)
1	ethanol	10	40
2	EtOH + H$_2$O (1:1)	10	60
3	MeOH	10	95
4	ACN	10	20
5	ACN + H$_2$O (3:0.3)	10	50
6	H$_2$O	10	no reaction

^{a}Reaction conditions: nitrobenzene (1 mmol), NaBH$_4$ (8 mmol), nanocatalyst (12 mg, 0.05 mmol), MeOH (5 mL) at RT. ^{b}Isolated yield: refers to yield after column chromatography (eluent: EtoAc/hexane 3:10).

Optimization of sodium borohydride: to investigate the effect of NaBH$_4$ on reaction conditions, different amounts of sodium borohydride were checked (2−10 mmol). Starting with 2 mmol of NaBH$_4$, there was a presence of the reactant in the reaction mixture. As the amount of NaBH$_4$ reached 8 mmol, the presence of a reactant disappears and the same

result is obtained with 10 mmol, which indicates that 8 mmol of $NaBH_4$ was enough to carry out the reaction at room temperature. The effect of $NaBH_4$ can be seen in Table 5. Thus, the optimum value of sodium borohydride for carrying out reaction efficiently is 8 mmol, and hence, the same amount was used for all the reactions.

Table 5. Effect of Concentration of $NaBH_4$ on the Reduction of Nitroarenes[a] Catalyzed by NCFP Nano-Ferrites

s. no.	$NaBH_4$ (mmol)	time (min)	yield (%)[b]
1	2	10	20
2	4	10	50
3	6	10	70
4	8	10	95
5	10	10	95

[a]Reaction conditions: nitrobenzene (1 mmol), nanocatalyst (12 mg, 0.05 mmol), in (MeOH 5 mL) at RT. [b]Isolated yield: refers to yield after column chromatography (eluent: EtoAc/hexane 3:10).

Optimization of a nanocatalyst: to find out the optimum amount of a catalyst required for the reduction of nitroarenes, the amount of a catalyst was optimized for the model reaction. The catalyst NCFP was used for optimization because of its higher surface area and smaller crystallite size. In this case, various amounts (0.02−0.15 mmol) were tested to obtain a maximum yield. 0.05 mmol of the catalyst was found to give excellent yield, and further increase in the catalyst did not increase the yield considerably. Therefore, the optimized value of the catalyst is 0.05 mmol or 12 mg. Table 6 depicts the effect of different amounts of the catalyst on the model reaction.

Table 6. Effect of Different Amounts of the Catalyst on the Reduction of Nitroarenes[a] Catalyzed by the NCFP Nanocatalyst
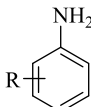
s. no.	catalyst	concentration (mmol)	yield (%)[b]
1	NCFP	0.02	60
2	NCFP	0.05	95
3	NCFP	0.1	95
4	NCFP	0.15	95

[a]Reaction conditions: nitrobenzene (1 mmol), $NaBH_4$ (8 mmol), nanocatalyst, MeOH (5 mL) at RT. [b]Isolated yield: refers to yield after column chromatography (eluent: EtoAc/hexane 3:10).

In summary, these observations showed that the best result for the reduction of nitrobenzene was obtained under conditions of $ArNO_2$ (1 mmol), $NaBH_4$ (8 mmol), and catalyst (12 mg or 0.05 mmol) in MeOH (5 mL) at RT (Scheme 2).

3.7.1.2. Extent of Catalytic Activity on Different Nitroarenes. Different nitro analogues were also used for the

Scheme 2. General Reaction for Reduction of Nitroarenes to Aminoarenes

R = CH_3, NH_2, OH, Cl.
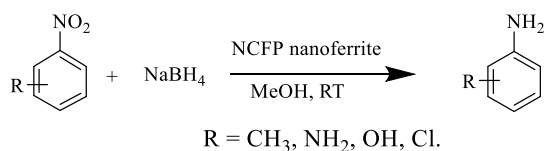
purpose of reduction in order to investigate the catalytic activity of prepared nano-ferrites. In all the nitro substrates, reaction conditions were kept the same as that of the model reaction and progress of the reaction was monitored by the TLC (eluent; EtOAc/hexane: 3/10). All the structures of amino arenes were elucidated by ^{1}HNMR and ^{13}CNMR, and data are given in Supporting Information Section S1. (1−9). Observed data of reduction of various nitro analogues are given in Table 7.

Table 7. Substrate Scope for the Reduction of Nitroarenes[a] to the Corresponding Aminoarenes Using $NaBH_4$ Catalysed by the NCFP Nanocatalyst

Entry	Reactant	Product	Time (min.)	Yield (%)[b]
1			10	95
2			10	75
3			10	75
4			10	90
5			10	80
6			10	85
7			10	95
8			10	80
9			10	90

[a]Reaction conditions: nitrobenzene (1 mmol), nanocatalyst (12 mg, 0.05 mmol), $NaBH_4$ (8 mmol) in (MeOH 5 ml) at RT. [b]Isolated yield: refers to yield after column chromatography (eluent; EtOAc/hexane 3:10).

3.7.1.3. Comparative Effect of NCFG, NCFP, and NCFU on the Catalytic Reduction of Nitroarenes. The reduction of nitroarenes with optimized conditions was checked for all the nano-ferrites prepared using different fuels. Here, in catalytic activity, a noticeable change has been observed. It was found that among the three catalysts, NCFP was giving the best yield of 95% in 10 min, which may be due to its high surface area. With NCFG as a catalyst, the yield is about 30% in 10 min. The low yield of the reaction product is mainly due to its very low surface area. While an increase in the yield was noticed with NCFU as catalyst but less than the NCFP giving 50% in 10 min as its surface area is intermediate between the two. Comparison of different NCF nanocatalysts is shown in Table 8. Our results of reduction of nitroarenes catalyzed by a NCFP

nanocatalyst were found to be much better than those reported earlier (Table 9).

Table 8. Comparison of Different Ferrites as Catalysts for the Reduction of Nitrobenzene[a] to Aniline

s. no.	catalyst	reaction time	yield (%)[b]
1	NCFP	10	95
2	NCFU	10	50
3	NCFG	10	30

[a]Reaction conditions: nitrobenzene (1 mmol), NaBH$_4$ (8 mmol), nanocatalysts (12 mg, 0.05 mmol), MeOH (5 mL) at RT. [b]Isolated yield: refers to yield after column chromatography (eluent: EtoAc/hexane 3:10).

3.7.1.4. Potential Mechanism for Reduction of Nitro-arenes. It is well established from the literature that spinel ferrites offer more fascinating catalytic activity in comparison to single component metallic oxides.[73] Mainly, catalytic activity depends upon the composition of a nanocatalyst. As reported earlier, for spinel ferrites, the catalytic performance depends on a number of factors like particle size, morphology of the nanocatalyst, surface area, redox nature of metal ions, and their distribution between tetrahedral (A) and octahedral (B) sites of cubic spinel crystal lattice. The metal ions which are present in the octahedral site play an important role in catalysis. This can be attributed to the well-known fact that octahedral sites are found to be exposed on the surface. In addition to this, metal ions present at octahedral sites are located at larger distances from which they can freely interact with the reactant molecules.[74] In the NCF nanoparticles, the Ni^{2+} ions preferably occupy the octahedral sites, which enhances the catalytic activity for the NCF ferrites.[75] NaBH$_4$ dissolves in methanol and ionizes, generating BH$_4^-$ ions. These BH$_4^-$ ions diffuse toward the catalyst and get adsorbed onto the NCFP nanocatalyst surface, which results in the formation of a metal−hydride (M−H) complex. Moreover, adsorption of nitro aromatic compounds onto the surface of the catalyst also takes place with reversible adsorption and desorption. Then, the hydride transfer from the M−H complex to nitroarenes takes place.[72,76] The hydride transfer was possible due to the presence of metal ions in the octahedral sites, wherein an electron transfer takes place between the ions present at the octahedral site. The nitroarenes reduces to their corresponding

amino arenes, followed by desorption of the final product from the catalyst surface. The surface of catalyst turns out to be free for further reaction. Figure 7 shows the pictorial representation of a possible mechanism.

3.7.2. Photo-Oxidative Degradation of Dye. The major type of pollutants present in the waste water from textile industries is the dye pollutants. Therefore, to investigate the photocatalytic behavior of the prepared nano-ferrites photo-oxidative degradation of model dye RhB is carried out under visible light.

3.7.2.1. Control Experiments. Different components used in the photo-oxidative degradation of RhB are hydrogen peroxide (H$_2$O$_2$), ferrite catalyst (NCFP), and a source of visible light. Before optimizing the reaction conditions, various sets of control experiments were done to visualize the role of different components on the photo-degradation of RhB. Reactions were done to study the individual effect of hydrogen peroxide (H$_2$O$_2$), NCF nanoparticles, and visible light on degradation of RhB. Figure 8a displays the various sets of experiments in the presence of dye + light only, dye + light + H$_2$O$_2$, NCFP + dye + light, and NCFP + dye + light + H$_2$O$_2$. It can be depicted from Figure 8a that degradation efficiency is very less (1.2%), when the reaction was performed with dye + visible light only. The degradation of RhB increases slightly when the reaction was carried out in the presence of only NCFP catalyst/H$_2$O$_2$ only, that is, 4.66 and 5.04%, respectively. This negligible degradation of RhB observed with H$_2$O$_2$ only is due to the limited oxidation capability of H$_2$O$_2$ ($E°$ = 1.76 V/SHE).[77,78] Degradation efficiency increased and reached a value of 92%, when the reaction was carried with dye + NCFP + H$_2$O$_2$ in the absence of visible light. It should be pointed out here that the degradation of RhB even in the presence of a NCFP catalyst is not enhanced unless the H$_2$O$_2$ is added in the reaction mixture. Usually in Fenton or Fenton-like reactions, the Fe^{2+} is oxidized by the H$_2$O$_2$ and the strongest oxidant, that is, OH$^•$ radicals are formed as an intermediate product, which can oxidize most of the organic pollutants in the water.[79] This 92% degradation of RhB in dark conditions clearly demonstrates that the NCFP nanocatalyst is an efficient heterogenous catalyst for Fenton or Fenton-like reactions. Further, under the illumination of visible light, the degradation efficiency improved to a maximum value of 99%, which could be due to the synergistic effect of photocatalysis and heterogeneous Fenton-like catalysis. Since the maximum efficiency of degradation was obtained under the

Table 9. Comparison of Catalytic Activity of NCFP Nanocatalysts with Some Recent Published Work

| Product	Catalyst	Reaction time(min)	Reaction conditions	Yield %	references
NH$_2$ R⧾⟨benzene ring⟩	CuFe$_2$O$_4$-graphene	30	PhNO$_2$(1 mmol), NaBH$_4$ (5 eq.), Catalyst (20mg), EtOH/H$_2$O, 70 °C, reflux.	92	26
	CuFe$_2$O$_4$	10	PhNO$_2$(1 mmol), NaBH$_4$ (2eq.), Catalyst (48 mg), H$_2$O, reflux.	95	27
	NiFe$_2$O$_4$@Cu	1	PhNO$_2$(1 mmol), NaBH$_4$ (2.5eq.),Catalyst(150mg), EtOH/H$_2$O, 80 °C	95	28
	Cu/SiO$_2$@NiFe$_2$O$_4$	90	PhNO$_2$(0.2 mmol), NaBH$_4$ (10 eq.), Catalyst (2.5mg), MeOH/H$_2$O, RT	95	29
	NiCrFeO$_4$	10	PhNO$_2$(1 mmol), NaBH$_4$ (8eq.) Catalyst (12 mg) MeOH, RT	95	This work
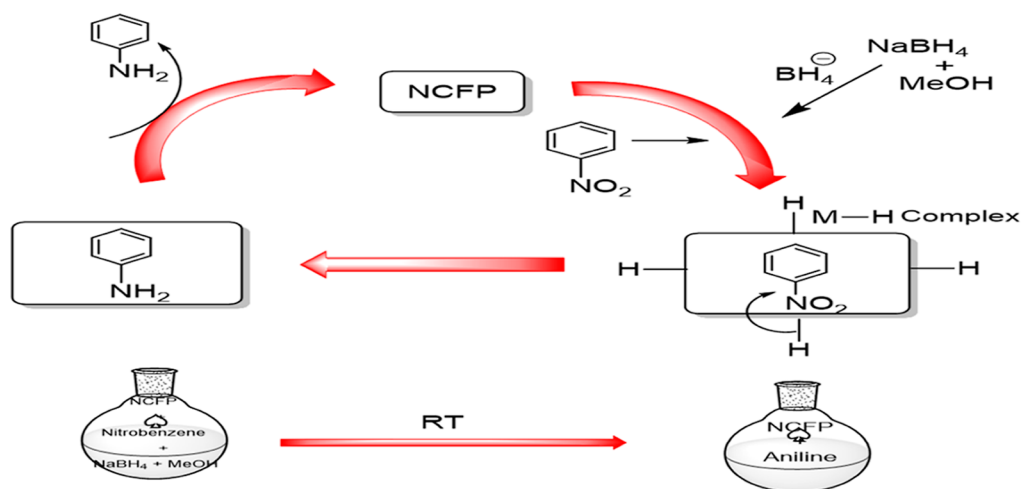
Figure 7. Pictorial representation of the mechanism of reduction of nitrobenzene to aniline.

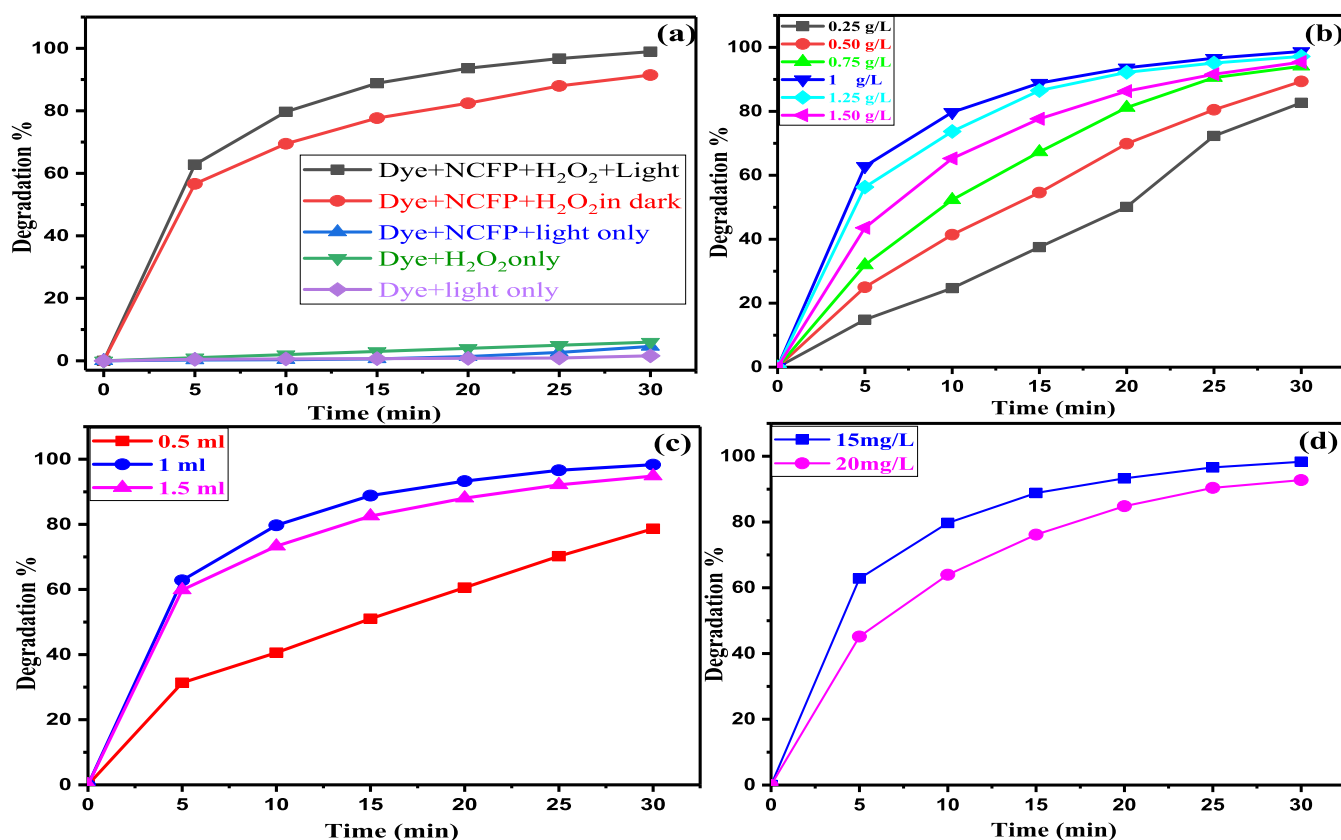**Figure 8.** (a) Control experiments for the degradation of RhB dye, optimization of various reaction parameters: (b) catalyst dosage, (c) H_2O_2, and (d) initial dye concentration toward maximum degradation of RhB.

illumination of visible light, all the components were optimized under the visible light-assisted degradation of RhB.

3.7.2.2. Optimization of Various Components. To obtain the optimal amount of different components like initial dye concentration, catalyst loading, and H_2O_2 dosage toward maximum degradation efficiency, optimization of these components was done for the photo-oxidative degradation of RhB dye using NCFP nanoferrite as a catalyst.

Catalyst loading: to determine the best and optimum amount of the catalyst required for maximum degradation efficiency, the concentration of the NCFP catalyst was varied from 0.25 to 1.25 g/L by keeping all the other components

constant (H_2O_2 = 1 mL, [dye] = 15 mg/L, 100 mL solution). In the beginning, with the increase in concentration from 0.25 to 1 g/L of the NCFP catalyst, the degradation efficiency increases from 82 to 99% in 30 min. This is because of the increase in the number of active sites of the catalyst. However, further increment in the concentration of the NCFP catalyst slows down the degradation process and degradation efficiency decreases from 99 to 96 and 95% for 1.25 and 1.5 g/L. The reason for this slow degradation is the increase in the turbidity of the reaction solution, which leads to lesser penetration of light and thereby slowdown of the process.[80] Since the maximum degradation efficiency is recorded with 1 g/L
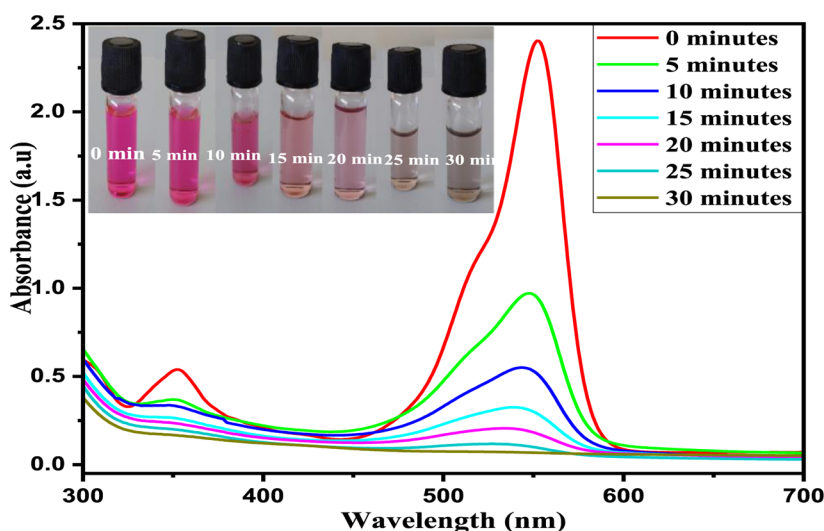
Figure 9. Typical UV−visible spectra for the photo-oxidative degradation of RhB.

concentration, all the degradation reactions were done with 1 g/L concentration of the NCFP catalyst. The variation of the NCFP catalyst with degradation efficiency is given in Figure 8b.

H$_2$O$_2$ dosage: the oxidant dosage also plays an important role in the photo-oxidative degradation of dyes. To investigate the optimum amount of H$_2$O$_2$, the reactions were performed with different concentrations of H$_2$O$_2$ (0.5, 1 and 1.5 mL), while all other variables were kept constant ([dye] = 15 mg/L, NCFP catalyst = 1 g/L). The increase in the degradation was observed when the amount increases from 0.5 to 1 mL, which might be due to increase in the number of OH$^{\bullet}$ produced, while above 1 mL scavenging of active OH$^{\bullet}$ occurred, as shown in eqs 6 and 7, which drops the degradation efficiency to a lower value.[81,82] The variation of different quantities of H$_2$O$_2$ with degradation efficiency is displayed in Figure 8c.

$$OH^{\bullet} + H_2O_2 \rightarrow H_2O + HOO^{\bullet} \tag{6}$$

$$OH^{\bullet} + HOO^{\bullet} \rightarrow H_2O + O_2 \tag{7}$$
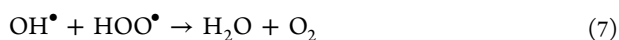
Therefore, the maximum efficiency was achieved with 1 mL of H$_2$O$_2$. Hence, this amount was taken as the optimized one and used for other reactions.

Initial dye concentration: to study the effect of initial dye concentration on the degradation efficiency, various initial concentrations (15 and 20 mg/L) of RhB dye were taken. However, all the other variables are kept constant, that is, H$_2$O$_2$ = 1 mL, NCFP catalyst = 1 g/L. Higher degradation efficiency was obtained for 15 mg/L within 30 min and the degradation efficiency decreased for the concentrations above 15 mg/L. The photo-degradation of different concentrations of RhB is shown in Figure 8d The decrease in the degradation efficiency for 20 mg/L concentration dye can be explained based on the fact that the production of hydroxyl radicals (OH$^{\bullet}$) in the solution was limited and the quantity of dye molecules was increased, which reduces the degradation efficiency for higher concentrations. Another reason for reduced degradation efficiency might be described by the Beer−Lambert law, according to which, with increase in the dye concentration, a decrease in the path length of photons entering solution was observed, which reduces the degradation efficiency.[83,84] Since the maximum efficiency is observed with

15 mg/L therefore, this concentration was taken as the optimized concentration for the remaining reactions.
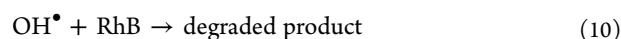
Furthermore, the same optimized conditions were utilized for MB, MO, and mixture of dyes (RhB, MO, and MB).
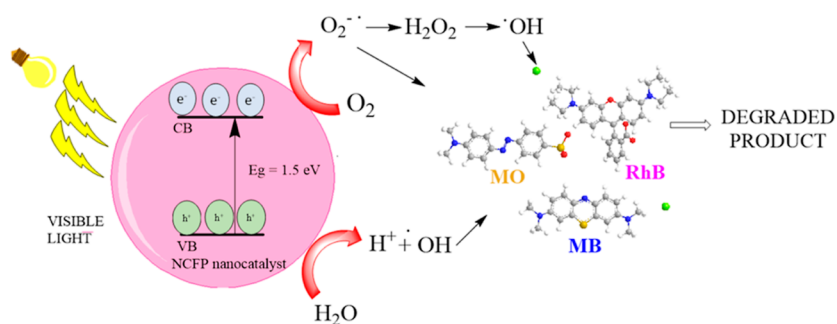
3.7.2.3. UV−Visible Spectroscopy. The UV−visible absorption maxima for RhB, MB, and MO dye were observed at 554, 664, and 464 nm, respectively, which gradually decreases down with an increase in time irradiation and almost disappears with NCF nanoparticles as catalysts. In addition to this, diminishing of the peak at absorption maxima is observed without the appearance of a new band in the UV or visible region, indicating the complete degradation of organic dyes. The rapid decrease in the intensity of the peak may be attributed to the breakdown of chromophores which are responsible for color in dyes. The graph of degradation of RhB using the optimized conditions is shown in Figure 9. The degradation efficiency (% degradation) at given time is calculated using the relation[85]

$$\% \text{ degradation} = \left(\frac{A_o - A_t}{A_o} \right) \times 100 \tag{8}$$

where A_o is the initial absorption intensity of the dye solution and A_t is the absorption intensity at time "t".

3.7.2.4. Mechanism of Fenton and Photo Fenton-like Degradation of RhB Dye. Fenton-like catalysis: the oxidative degradation of RhB dye occurs by a Fenton-like process by the addition of H$_2$O$_2$ and NCFP nanoparticles. As discussed earlier, the degradation efficiency in the dark or Fenton-like process is 92%, which might be due to the presence of active metal ions at octahedral sites and high surface area of the NCFP nanoparticles. It is the metal ions in the NCFP which are responsible for the decomposition of H$_2$O$_2$, improving the degradation up to 92% even in the absence of visible light. The Fe^{3+} active sites on the surface of a NCFP catalyst were reduced to form Fe^{2+} active sites, which then reacted with H$_2$O$_2$ to produce Fe^{3+} and OH$^{\bullet}$ radicals.[86] The conversion of Fe^{3+} to Fe^{2+} is greatly enhanced by the Cr^{2+} ions, which could be produced by the reduction with H$_2$O$_2$ or HO$_2^{\bullet}$ (eqs 9−12).[87]

$$H_2O_2 + Fe^{2+} \rightarrow Fe^{3+} + OH^{\bullet} + OH^{-} \tag{9}$$

$$OH^{\bullet} + RhB \rightarrow \text{degraded product} \tag{10}$$

Figure 10. Pictorial representation of the mechanism of degradation of dyes with NCFP as a catalyst and H_2O_2 as an oxidant.

$$HO_2^{\bullet} + Cr^{3+} \rightarrow Cr^{2+} + O_2 + H^+ \qquad (11)$$

$$Fe^{3+} + Cr^{2+} \rightarrow Fe^{2+} + Cr^{3+} \qquad (12)$$
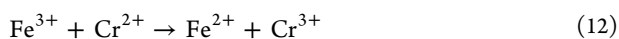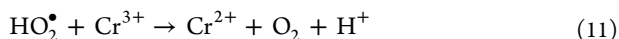
Thus, in the dark conditions, a Fenton-like heterogenous catalysis is observed and hence the degradation of RhB occurs.

Photo-Fenton or photo-oxidative degradation: the pictorial diagram of the mechanism of degradation of dye is shown in Figure 10. In addition to the Fenton-like reaction or in the dark condition, when the reaction is carried out under the visible light, the degradation efficiency increases to 99%. Initially the visible light falls on the NCFP photocatalyst surface, which activates NCFP, and pairs of e_{cb}^-/h_{vb}^+ are generated because of its narrow band gap energy (1.5 eV). When the visible light is absorbed by the NCFP nanocatalyst, electrons from the valence band get excited and migrated to the conduction band, while the holes are left in the valence band.[88] The photogenerated h_{vb}^+ in the valence band combines with the water molecules to form $OH^{\bullet}$, which is responsible for degradation of RhB dye or can direct oxidize the dye.[89] Moreover, the photogenerated electrons in the conduction band of NCFP nanoparticles combines with the adsorbed O_2 molecules to form $O_2^{-\bullet}$, which directly reacted with the dye or combined with H_2O_2 to produce $OH^{\bullet}$,[80] which degrade the dye and the reaction solution become colorless, as shown in Figure 9. Thus, the photo-degradation efficiency of the hazardous and toxic dyes is enhanced by photo-Fenton-like process due to generation of more amounts of $OH^{\bullet}$ radicals. Hence, it can be concluded that overall photodegradation of dyes is due to the combined effect of Fenton-like heterogeneous catalysis and photocatalysis.

3.7.2.5. PL Properties. Photocatalytic activity has a strong correlation with the PL intensity, that is, the lower the PL intensity, the higher will be the photocatalytic performance and vice versa.[90] The PL spectra of nanocatalysts were recorded at room temperature with excitation wavelength of 325 nm and displayed in Figure 11. Mostly, the PL spectroscopy is employed to study the transfer, migration, and recombination processes, as these originate from the recombination of free charge carriers, that is, e_{cb}^-/h_{vb}^+.[91] It is observed from the PL spectrum that the all the NCF nanocatalysts show an emission peak at 653 nm in the visible region. It is concluded from the literature that the PL emission intensity is the result of recombination of photogenerated charge carriers.[92,93] NCFG gives the highest intensity peak in the PL spectrum ,which is due to the highest rate of recombination of electron−hole and hence shows the least photocatalytic activity.[94] Furthermore, a decrease in the intensity of NCFU is observed and photocatalytic activity changes accordingly. A significant decrease is seen in the peak intensity of the sample NCFP nanoparticle,
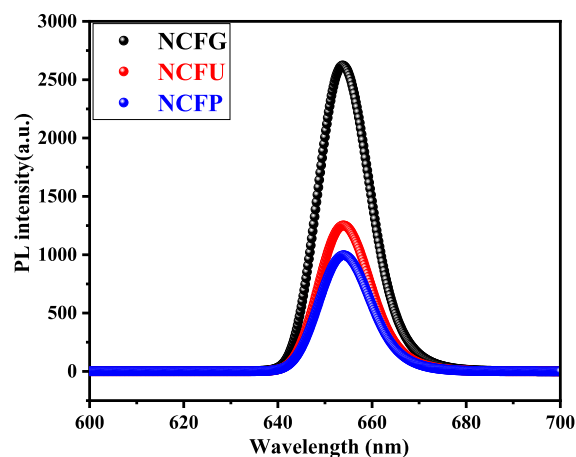
Figure 11. PL spectra of NCFP, NCFG and NCFU recorded at room temperature.

indicating effective suppression of photogenerated charge carriers.

3.7.2.6. Comparative Effect of NCF Nano-Ferrites on Photocatalytic Degradation of Organic Dyes and Their Mixture. The comparative effect of the nano photocatalysts, that is, NCFP, NCFU, and NCFG was studied on the photocatalytic degradation of RhB, MB, MO, and their mixture using optimized reaction conditions, the results of which are presented in Figure 12. It was observed that the degradation efficiency of individual dye was highest with NCFP (99%) in 30 min for RhB, 50 min for MB, and 115 min for MO dye. For a NCFU catalyst, the 99% of degradation was achieved for RhB in 85 min, 75 min for MB, and 160 min for MO dye. The NCFG catalyst did not degrade RhB dye completely and reached a limiting value of 27% in 220 min, and only 2−3% of degradation was achieved for MO and 2% for MB in 130 min, after which the degradation % remained constant. The difference in degradation efficiency of different photo-catalysts can be explained on the basis of surface area, band gap, and PL spectra. The highest surface area is observed for the NCFP, and the same trend was observed in the photodegradation of the dyes because catalytic activity is largely dependent on the surface area.[47] Furthermore, it is well known in the literature that the lower the band gap, the higher is the photocatalytic activity due to facile excitation of photogenerated electrons.[95,96] As the band gap value for NCFP is smaller than all the other photocatalysts, this could be the reason for its higher photocatalytic activity. Also, the highest photocatalytic activity of NCFP is supported by the PL studies. The PL emission intensity results from the recombination of photo-
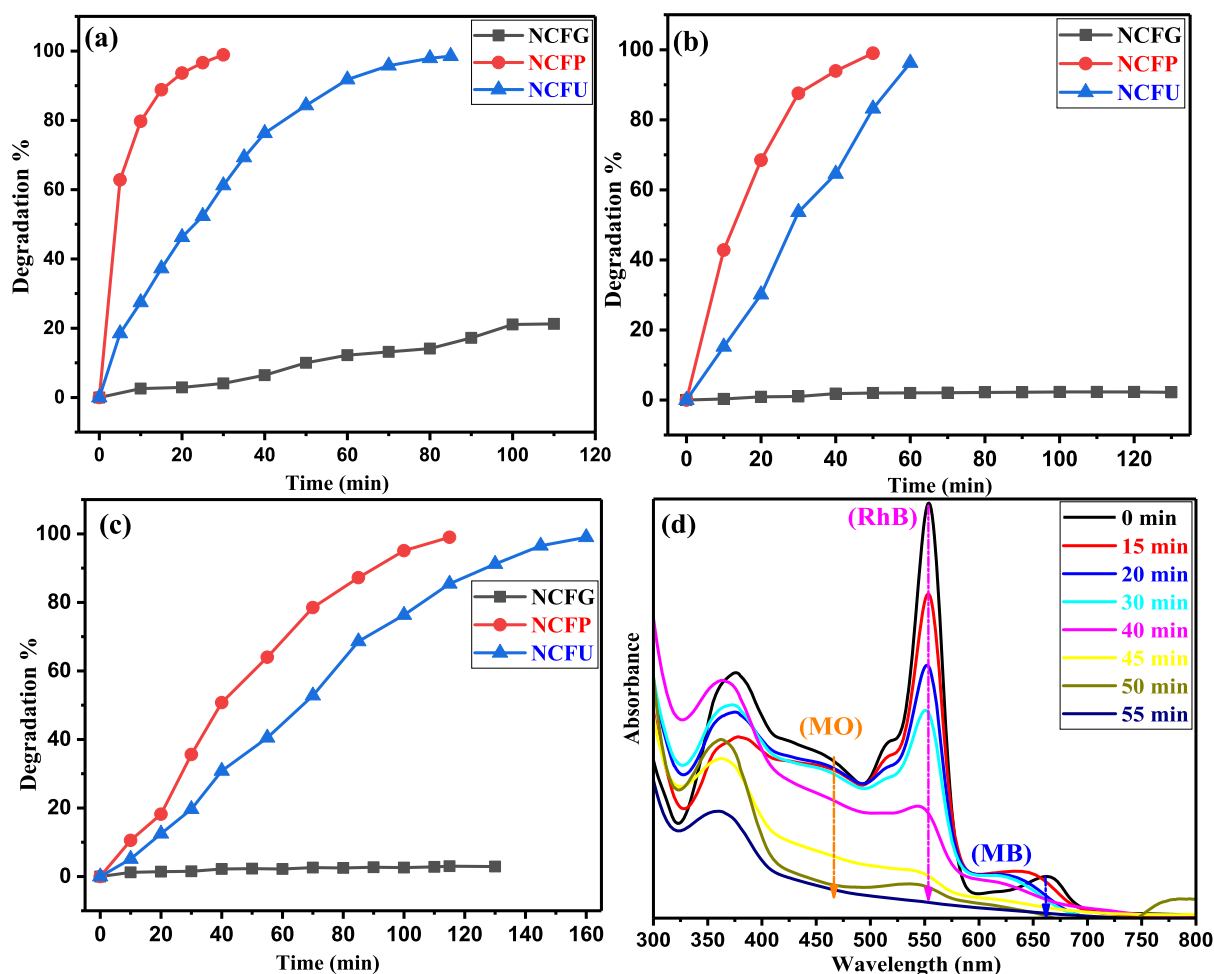
Figure 12. Comparison of NCF nanocatalysts with different dyes and time: (a) RhB, (b) MB, (c) MO, and (d) time-dependent spectral changes in photodegradation of mixture of dyes (RhB, MO, and MB) with NCFP as a catalyst.

Table 10. Comparison of Photocatalytic Activity of the NCFP Catalyst with Some Published Photocatalysts

s. no	catalyst	reaction condition	degradation time (min)/degradation (%)	references
1	$Ni_{0.4}Cu_{0.6}Fe_2O_4$	RhB = 9 mg/L, pH = 2, H_2O_2	210/99	31
2	$NiFe_2O_4$@HAp-Sn^{2+}	RhB = 10 mg/L, H_2O_2	40/99	32
3	$NiFe_2O_4$@SiO_2	RhB = 10 mg/L, pH = 7, H_2O_2	480/72.8	33
4	$NiFe_2O_4$	RhB = 10 mg/L, pH = 3 oxalic acid	60/98.7	34
5	$CoFe_2O_4$-rGO	RhB = 25 mg/L, MB = 30 mg/L and MO = 20 mg/L, H_2O_2	120/99 (mixture)	35
6	$NiFeCrO_4$	RhB, MB, MO = 15 mg/L, H_2O_2	30/99 (RhB), 55/99 (RhB in the mixture), 50/99 (MB in the mixture), 55/89 (MO in the mixture)	this work

generated e_{cb}^-/h_{vb}^+. As discussed earlier, the lower PL intensity in the case of NCFP enhances the photodegradation of dye, suppressing the combination of electrons and holes, and thus provides a large number of charge carriers for the reaction. Hence, from the abovementioned discussion, the best catalyst for photo-oxidative degradation of organic dyes in their unitary solutions is NCFP and shows tremendous activity.

In the case of the mixture of dyes, the NCFP nanocatalyst degrades MB and RhB completely in 50 and 55 min, respectively, whereas the MO dye degraded up to 89% in 55 min and further exposure of light did not cause any change in the absorbance of MO dye (Figure 12d). Here, in the case of NCFU, the same trend is observed for MO in the mixture of dyes, that is, only 84% degradation was achieved and thereafter

remained constant, whereas MB and RhB dyes were completely degraded in 70 and 80 min, respectively. The NCFG catalyst did not show much degradation (RhB = 4%, MO = 11%, MB = 2%). It may be noted that compared to other two dyes, MO is not completely degraded by NCFP and NCFU, indicating clearly that the degradations of these dyes would be competitive reactions due to their cationic and anionic nature.[97] As the NCFP and NCFU catalysts are supposed to be electron-abundant materials, which can easily attract the cationic dye involving RhB and MB, MO dye is not degraded completely and is considered to be anionic in nature. The photocatalytic performance of the catalyst NCFP was found to be superior to the catalysts reported in the literature, and their comparison is shown in Table 10.
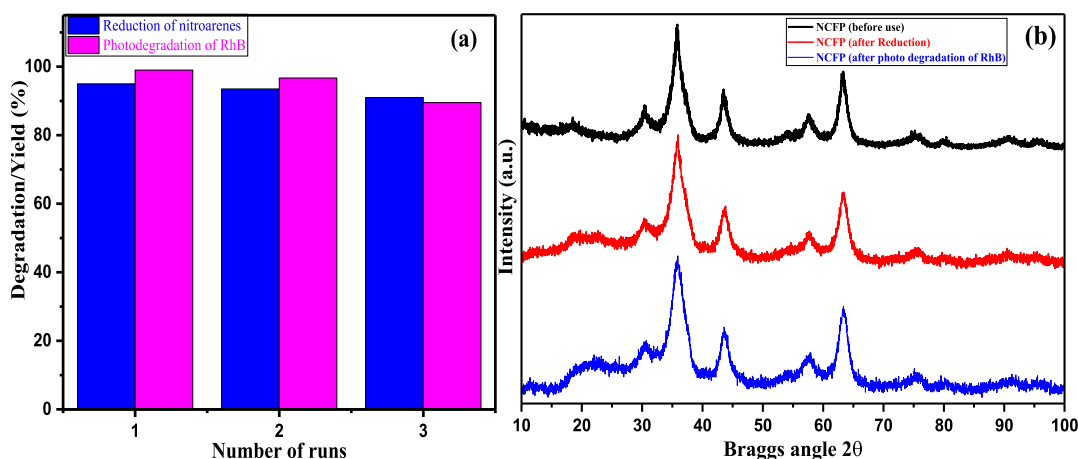
Figure 13. (a) Recyclability of the NCFP catalyst after three runs and (b) XRD diffractograms of an NCFP nanocatalyst before and after recyclability from reduction and photodegradation of RhB.

3.8. Recyclability and Stability of the NCFP Catalyst.

Recycling of the catalyst is a very important factor for heterogeneous catalytic reactions. Recyclability of the catalyst in both reduction and photo-oxidative degradation reaction was tested. In reduction, nitrobenzene was chosen as the reactant for recyclability reaction. The NCFP catalyst was recovered by simple filtration and washed with water and ethanol several times to remove any absorbed organic compound and then dried in an oven before use for the next cycle. Also, the amount of the reactant taken in the next cycle was adjusted according to the recovered catalyst. For up to three consecutive cycles, a slight decrease in yield from 95% to 91% was observed, which clearly indicates that the catalyst can be used again and again (Figure 13a). In photo-oxidative degradation, RhB dye was chosen as the model dye, and the catalyst was recovered by centrifugation and then washed with water and ethanol to remove any dye molecules. Before using in the next cycle, the catalyst was heated in an oven at 120 °C for 1 h to remove water from the catalyst. The degradation efficiency decreased from 99% to 89% in three cycles, demonstrating the stability of the catalyst. The XRD diffractograms of the recovered samples are shown in Figure 13b. From the XRD graphs, it can be depicted that no deformation in the catalyst phase was observed and possibility for a slight decrease in catalytic activity due to the leaching of metal ions is ruled out. The decrease in catalyst activity might be due to the loss of the sample during the separation process.[98]

4. CONCLUSIONS

$NiCrFeO_4$ ferrite nanoparticles have been successfully synthesized by the combustion method using glycine (NCFG), PVA (NCFP), and urea (NCFU) as fuel. In spite of the same composition, a significant variation in the structural, morphology, surface, optical, magnetic, and catalytic properties has been found. Among the prepared nanoparticles, NCFP was found to possess the lowest particle size (5.5 nm) and highest surface area (90.9 m^2/g), while the highest M_s and coercivity values were shown by NCFG nanoparticles. Due to its higher surface area and low band gap, NCFP showed excellent catalytic activity for reduction of nitroarenes at room temperature in 10 min with good yield and about 99% photodegradation of RhB in quick time (30 min) [MB (50 min) and MO (115 min)]. Moreover, the NCFP nanocatalyst

was found to be degrading the mixture of dyes (RhB, MO, and MB) quite efficiently in less time as compared to NCFU and NCFG. The stability and recyclability with no significant loss in catalytic and photocatalytic performance up to three runs made it a versatile candidate for industrial use and for cleaning of the environment.

■ ASSOCIATED CONTENT

Ⓢ Supporting Information

The Supporting Information is available free of charge at https://pubs.acs.org/doi/10.1021/acsomega.2c01616.

Powder XRD diffractograms of NCF nanoparticles, EDX spectrum of all the synthesized nanoparticles, N_2 adsorption−desorption isotherm of all the nanocatalysts, ^{1}HNMR and ^{13}CNMR spectra of aniline and *p*-aminophenol, and spectral details of all the amino-arenes obtained by the reduction of nitro-arenes catalyzed by NCFP nanoparticles (PDF)

■ AUTHOR INFORMATION

Corresponding Author

Devinder Singh — *Department of Chemistry, University of Jammu, Jammu 180006, India;* Ⓘ orcid.org/0000-0002-2741-302X; Email: drdssambyal@rediffmail.com

Authors

Sumit Singh — *Department of Chemistry, University of Jammu, Jammu 180006, India*

Shikha Sharma — *Department of Chemistry, University of Jammu, Jammu 180006, India*

Ujwal Manhas — *Department of Chemistry, University of Jammu, Jammu 180006, India*

Irfan Qadir — *Department of Chemistry, University of Jammu, Jammu 180006, India*

Amit Kumar Atri — *Department of Chemistry, University of Jammu, Jammu 180006, India*

Complete contact information is available at:
https://pubs.acs.org/10.1021/acsomega.2c01616

Notes

The authors declare no competing financial interest.

■ REFERENCES

(1) Wang, H.; Huang, J.; Ding, L.; Li, D.; Han, Y. A facile synthesis of monodisperse $CoFe_2O_4/SiO_2$ nanoparticles. *Appl. Surf. Sci.* **2011**, *257*, 7107−7112.

(2) Basti, H.; Ben Tahar, L.; Smiri, L. S.; Herbst, F.; Vaulay, M.-J.; Chau, F.; Ammar, S.; Benderbous, S. Catechol derivatives-coated Fe_3O_4 and γ-Fe_2O_3 nanoparticles as potential MRI contrast agents. *J. Colloid Interface Sci.* **2010**, *341*, 248−254.

(3) Wen, C.; Yin, A.; Dai, W.-L. Recent advances in silver-based heterogeneous catalysts for green chemistry processes. *Appl. Catal., B* **2014**, *160−161*, 730−741.

(4) Centi, G.; Perathoner, S. Catalysis and sustainable (green) chemistry. *Catal. Today* **2003**, *77*, 287−297.

(5) Menini, L.; Pereira, M.; Parreira, L.; Fabris, J.; Gusevskaya, E. Cobalt and manganese-substituted ferrites as efficient single-site heterogeneous catalysts for aerobic oxidation of mono-terpenic alkenes under solvent-free conditions. *J. Catal.* **2008**, *254*, 355−364.

(6) Lin, X.; Zhang, Y.; Yin, L.; Chen, C.; Zhan, Y.; Li, D. Characterization and catalytic performance of copper-based WGS catalysts derived from copper ferrite. *Int. J. Hydrogen Energy* **2014**, *39*, 6424−6432.

(7) Gholinejad, M.; Karimi, B.; Mansouri, F. Synthesis and characterization of magnetic copper ferrite nanoparticles and their catalytic performance in one-pot odourless carbon-sulfur bond formation reactions. *J. Mol. Catal. Chem.* **2014**, *386*, 20−27.

(8) Jauhar, S.; Singhal, S.; Dhiman, M. Manganese substituted cobalt ferrites as efficient catalysts for H_2O_2 assisted degradation of cationic and anionic dyes: their synthesis and characterizatio. *Appl. Catal., A* **2014**, *486*, 210−218.

(9) Roonasi, P.; Nezhad, A. Y. A comparative study of a series of ferrite nanoparticles as heterogeneous catalysts for phenol removal at neutral Ph. *Mater. Chem. Phys.* **2016**, *172*, 143−149.

(10) Boudjemaa, A.; Popescu, I.; Juzsakova, T.; Kebir, M.; Helaili, N.; Bachari, K.; Marcu, I.-C. M-substituted (M= Co, Ni and Cu) zinc ferrite photo-catalysts for hydrogen production by water photo-reduction. *Int. J. Hydrogen Energy* **2016**, *41*, 11108−11118.

(11) Tsoncheva, T.; Manova, E.; Velinov, N.; Paneva, D.; Popova, M.; Kunev, B.; Tenchev, K.; Mitov, I. Thermally synthesized nanosized copper ferrites as catalysts for environment protection. *Catal. Commun.* **2010**, *12*, 105−109.

(12) Satish, G.; Reddy, K. H. V.; Anil, B. S. P.; Ramesh, K.; Kumar, R. U.; Nageswar, Y. V. D. Direct C−H arylation of benzothiazoles by magnetically separable nano copper ferrite, a recyclable catalyst. *Tetrahedron Lett.* **2015**, *56*, 4950−4953.

(13) Yadav, R. S.; Kuřitka, I.; Vilcakova, J.; Havlica, J.; Masilko, J.; Kalina, L.; Tkacz, J.; Enev, V.; Hajdúchová, M. Structural, magnetic, dielectric, and electrical properties of NiFe2O4 spinel ferrite nanoparticles prepared by honey-mediated sol-gel combustion. *J. Phys. Chem. Solids* **2017**, *107*, 150−161.

(14) Pradhan, N.; Pal, A.; Pal, T. Silver Nanoparticle Catalyzed Reduction of Aromatic Nitro Compounds. *Colloids Surf., A* **2002**, *196*, 247−257.

(15) Ai, L.; Jiang, J. Catalytic reduction of 4-nitrophenol by silver nanoparticles stabilized on environmentally benign macroscopic biopolymer hydrogel. *Bioresour. Technol.* **2013**, *132*, 374−377.

(16) Chang, Y.-C.; Chen, D.-H. Catalytic reduction of 4-nitrophenol by magnetically recoverable Au nanocatalyst. *J. Hazard. Mater.* **2009**, *165*, 664−669.

(17) Koga, H.; Kitaoka, T. One-step synthesis of gold nanocatalysts on a micro structured paper matrix for the reduction of 4-nitrophenol. *Chem. Eng. J.* **2011**, *168*, 420−425.

(18) Chiou, J.-R.; Lai, B.-H.; Hsu, K.-C.; Chen, D.-H. One-pot green synthesis of silver/iron oxide composite nanoparticles for 4-nitrophenol reduction. *J. Hazard. Mater.* **2013**, *248−249*, 394−400.

(19) Basu, B.; Das, P.; Das, S. Transfer hydrogenation using recyclable polymer-supported formate (PSF): Efficient and chemoselective reduction of nitroarenes. *Mol. Divers.* **2005**, *9*, 259−262.

(20) He, Y.; Lei, C.; Lin, Q.; Dong, J.; Yu, Y.; Wang, L. Mössbauer and Structural properties of La-substituted $Ni_{0.4}Cu_{0.2}Zn_{0.4}Fe_2O_4$ nanocrystalline ferrite. *Sci. Adv. Mater.* **2015**, *7*, 1809−1815.

(21) Lohar, K. S.; Patange, S. M.; Mane, M. L.; Shirsath, S. E. Cation distribution investigation and characterizations of $Ni_{1−x}Cd_xFe_2O_4$ nanoparticles synthesized by citrate gel process. *J. Mol. Struct.* **2013**, *1032*, 105−110.

(22) Jacobs, J. P.; Maltha, A.; Reintjes, J. G. H.; Drimal, J.; Ponec, V.; Brongersma, H. H. The surface of catalytically active spinels. *J. Catal.* **1994**, *147*, 294−300.

(23) Patange, S. M.; Shairsarh, S. E.; Jadhav, S. S.; Lohar, K. S.; Mane, D. R.; Jadhav, K. M. Rietveld refinement and switching properties of Cr^{3+} substituted $NiFe_2O_4$ ferrites. *Mater. Lett.* **2010**, *64*, 722−724.

(24) Ganure, K. A.; Langade, M. M.; Dhale, L. A.; Lohar, K. S. Chromium substituted nickel ferrites ($NiFe_{2−x}Cr_xO4$, x= 0.0, 0.1, 0.2, 0.3,and 0.4) magnetically recoverable reusable heterogeneous nano catalysts. *Mater. Today* **2021**, *46*, 6139−6144.

(25) Singhal, S.; Chandra, K. Cation distribution and magnetic properties in chromium substituted nickel ferrites prepared using aerosol route. *J. Solid State Chem.* **2007**, *180*, 296−300.

(26) Zhang, H.; Gao, S.; Shang, N.; Wang, C.; Wang, Z. Copper ferrite−graphene hybrid: a highly efficient magnetic catalyst for chemoselective reduction of nitroarenes. *RSC Adv.* **2014**, *4*, 31328−31332.

(27) Zeynizadeh, B.; Farkhondeh, M. A.; Mousavi, H. Green and convenient protocols for the efficient reduction of nitriles and nitro compounds to corresponding amines with $NaBH_4$ in water catalyzed by magnetically retrievable $CuFe_2O_4$ nanoparticles. *Res. Chem. Intermed.* **2019**, *45*, 3329−3357.

(28) Zeynizadeh, B.; Mohammadzadeh, I.; Shokri, Z.; Ali Hosseini, S. Synthesis and characterization of $NiFe_2O_4@Cu$ nanoparticles as a magnetically recoverable catalyst for reduction of nitroarenes to arylamines with $NaBH_4$. *J. Colloid Interface Sci.* **2017**, *500*, 285−293.

(29) Parmekar, M. V.; Salker, A. V. Room temperature complete reduction of nitroarenes over a novel $Cu/SiO_2@NiFe_2O_4$ nano-catalyst in an aqueous medium−a kinetic and mechanistic study. *RSC Adv.* **2016**, *6*, 108458−108467.

(30) Liang, X.; Zhong, Y.; He, H.; Yuan, P.; Zhu, J.; Zhu, S.; Jiang, Z. The application of chromium substituted magnetite as heterogeneous Fenton catalyst for the degradation of aqueous cationic and anionic dyes. *Chem. Eng. J.* **2012**, *191*, 177−184.

(31) Dhiwahar, A. T.; Maruthamuthu, S.; Marnadu, R.; Sundararajan, M.; Manthrammel, M. A.; Shkir, M.; Sakthivel, P.; Minnam Reddy, V. R. Improved photocatalytic degradation of rhodamine B under visible light and magnetic properties using microwave combustion grown Ni doped copper ferrite spinel nanoparticles. *Solid State Sci.* **2021**, *113*, 106542.

(32) Das, K. C.; Dhar, S. S.; Thakurata, D. G.; Das, J. Sn (II) inserted on hydroxyapatite encapsulated nickel ferrite ($NiFe_2O_4@$ HAp-Sn^{2+}): A novel nanocomposite for the effective photo-degradation of rhodamine B dye. *J. Clean. Prod.* **2021**, *290*, 125172.

(33) Qu, J.; Che, T.; Shi, L.; Lu, Q.; Qi, S. A novel magnetic silica supported spinel ferrites $NiFe_2O_4$ catalyst for heterogeneous Fenton-like oxidation of rhodamine B. *Chin. Chem. Lett.* **2019**, *30*, 1198−1203.

(34) Liu, S.-Q.; Feng, L.-R.; Xu, N.; Chen, Z.-G.; Wang, X.-M. Magnetic nickel ferrite as a heterogeneous photo-Fenton catalyst for the degradation of rhodamine B in the presence of oxalic acid. *Chem. Eng. J.* **2012**, *203*, 432−439.

(35) Moitra, D.; Chandel, M.; Ghosh, B. K.; Jani, R. K.; Patra, M. K.; Vadera, S. R.; Ghosh, N. N. A simple 'in situ'co-precipitation method for the preparation of multifunctional CoFe2O4−reduced graphene oxide nanocomposites: excellent microwave absorber and highly efficient magnetically separable recyclable photocatalyst for dye degradation. *RSC Adv.* **2016**, *6*, 76759−76772.

(36) Choudhary, S.; Hasina, D.; Saini, M.; Ranjan, M.; Mohapatra, S. Facile synthesis, morphological, structural, photocatalytic and optical properties of ZnFe2O4-ZnO hybrid nanostructures. *J. Alloys Compd.* **2022**, *895*, 162723.

(37) Lazarova, T.; Georgieva, M.; Tzankov, D.; Voykova, D.; Aleksandrov, L.; Cherkezova-Zheleva, Z.; Kovacheva, D. Influence of the type of fuel used for the solution combustion synthesis on the structure, morphology and magnetic properties of nanosized NiFe2O4. *J. Alloys Compd.* **2017**, *700*, 272−283.

(38) Rashad, M. M.; El-Shaarawy, M. G.; Shash, N. M.; Maklad, M. H.; Afifi, F. A. Controlling the composition, microstructure, electrical and magnetic properties of LiFe5O8powders synthesized by sol gel auto-combustion method using urea as a fuel. *J. Magn. Magn. Mater.* **2015**, *374*, 495−501.

(39) Jain, S. R.; Adiga, K. C.; Pai Verneker, V. R. A new approach to thermochemical calculations of condensed fuel-oxidizer mixtures. *Combust. Flame* **1981**, *40*, 71−79.

(40) Pacewska, B.; Keshr, M. Thermal transformations of aluminium nitrate hydrate. *Thermochim. Acta* **2002**, *385*, 73−80.

(41) Fang, H. L.; Dacosta, H. F. M. Urea thermolysis and NOx reduction with and without SCR catalysts. *Appl. Catal., B* **2003**, *46*, 17−34.

(42) Peña, A.; Gutiérrez, J.; Barandiarán, J. M.; Chapman, J. P.; Insausti, M.; Rojo, T. Correlation between structure and magnetic properties of Cd-substitutedLa $_{0.7}$(Ca$_{0.3−x}$Cd$_x$)MnO$_3$ CMR manganites. *J. Solid State Chem.* **2003**, *174*, 52−59.

(43) Larson, A. C.; VonDreele, R. B. *GSAS*; Los Alamos National Laboratory, 1994; pp 86−748.

(44) Qu, Y.; Yang, H.; Yang, N.; Fan, Y.; Zhu, H.; Zou, G. The effect of reaction temperature on the particle size, structure and magnetic properties of coprecipitated CoFe2O4 nanoparticles. *Mater. Lett.* **2006**, *60*, 3548−3552.

(45) Khorsand Zak, A.; Abd. Majid, W. H.; Abrishami, M. E.; Yousefi, R. X-ray analysis of ZnO nanoparticles by Williamson−Hall and size−strain plot methods. *Solid State Sci.* **2011**, *13*, 251−256.

(46) Phadatare, M. R.; Salunkhe, A. B.; Khot, V. M.; Sathish, C. I.; Dhawale, D. S.; Pawar, S. H. Thermodynamic, structural and magnetic studies of NiFe2O4 nanoparticles prepared by combustion method: Effect of fuel. *J. Alloys Compd.* **2013**, *546*, 314−319.

(47) Chung, W.-C.; Chang, M.-B. Review of catalysis and plasma performance on dry reforming of CH4 and possible synergistic effects. *Renewable Sustainable Energy Rev.* **2016**, *62*, 13−31.

(48) Abida, B.; Chirchi, L.; Baranton, S.; Napporn, T. W.; Kochkar, H.; Léger, J.-M.; Ghorbel, A. Preparation and characterization of Pt/TiO2 nanotubes catalyst for methanol electro-oxidation. *Appl. Catal., B* **2011**, *106*, 609−615.

(49) Cui, H.-J.; Shi, J.-W.; Yuan, B.; Fu, M.-L. Synthesis of porous magnetic ferrite nanowires containing Mn and their application in water treatment. *J. Mater. Chem. A* **2013**, *1*, 5902−5907.

(50) Sonar, S. K.; Niphadkar, P. S.; Mayadevi, S.; Joshi, P. N. Preparation and characterization of porous fly ash/NiFe2O4 composite: promising adsorbent for the removal of congo red dye from aqueous solution. *Mater. Chem. Phys.* **2014**, *148*, 371−379.

(51) Sun, M.-H.; Huang, S.-Z.; Chen, L.-H.; Li, Y.; Yang, X.-Y.; Yuan, Z.-Y.; Su, B.-L. Applications of hierarchically structured porous materials from energy storage and conversion, catalysis, photocatalysis, adsorption, separation, and sensing to biomedicine. *Chem. Soc. Rev.* **2016**, *45*, 3479−3563.

(52) Chaturvedi, S.; Das, R.; Poddar, P.; Kulkarni, S. Tunable band gap and coercivity of bismuth ferrite−polyaniline core−shell nanoparticles: the role of shell thickness. *RSC Adv.* **2015**, *5*, 23563−23568.

(53) Dom, R.; Subasri, R.; Hebalkar, N. Y.; Chary, A. S.; Borse, P. H. Synthesis of a hydrogen producing nanocrystalline ZnFe2O4 visible light photocatalyst using a rapid microwave irradiation method. *RSC Adv.* **2012**, *2*, 12782−12791.

(54) Almessiere, M. A.; Slimani, Y.; Korkmaz, A. D.; Guner, S.; Sertkol, M.; Shirsath, S. E.; Baykal, A. Structural, optical and magnetic properties of Tm^{3+} substituted cobalt spinel ferrites synthesized via sonochemical approach. *Ultrason. Sonochem.* **2019**, *54*, 1−10.

(55) Bharathi, K. K.; Noor-A-Alam, M.; Vemuri, R. S.; Ramana, C. V. Correlation between microstructure, electrical and optical properties of nanocrystalline NiFe$_{1.925}$Dy$_{0.075}$O$_4$ thin films. *RSC Adv.* **2012**, *2*, 941−948.

(56) Yuan, Z.-h.; Wei, Y.; Jun-hui, J.; Li-de, Z. Optical absorption red shift of capped ZnFe2O4 nanoparticle. *Chin. Phys. Lett.* **1998**, *15*, 535−537.

(57) Singh, J. P.; Srivastava, R. C.; Agrawal, H. M. Optical behaviour of zinc ferrite nanoparticles. *AIP Conf. Proc.* **2010**, *1276*, 137−143.

(58) Naik, M. M.; Naik, H. S. B.; Nagaraju, G.; Vinuth, M.; Vinu, K.; Rashmi, S. K. Effect of aluminium doping on structural, optical, photocatalytic and antibacterial activity on nickel ferrite nanoparticles by sol−gel auto-combustion method. *J. Mater. Sci. Mater. Electron.* **2018**, *29*, 20395−20414.

(59) Asiri, S.; Sertkol, M.; Guner, S.; Gungunes, H.; Batoo, K. M.; Saleh, T. A.; Sozeri, H.; Almessiere, M. A.; Manikandan, A.; Baykal, A. Hydrothermal synthesis of Co$_y$Zn$_y$Mn$_{1-2y}$Fe$_2$O$_4$ nanoferrites: magneto-optical investigation. *Ceram. Int.* **2018**, *44*, 5751−5759.

(60) Joshi, S.; Kumar, M.; Chhoker, S.; Srivastava, G.; Jewariya, M.; Singh, V. N. Structural, magnetic, dielectric and optical properties of nickel ferrite nanoparticles synthesized by co-precipitation method. *J. Mol. Struct.* **2014**, *1076*, 55−62.

(61) Gupta, K.; Komal, K. B.; Nidhi, V.; Tikoo, K. B.; Kumar, V.; Bansal, S.; Kaushik, A.; Singhal, S. Synchronous role of coupled adsorption and photocatalytic oxidation on the hybrid nanomaterials of pectin and nickel ferrite leads to the excellent removal of toxic dye effluents. *New J. Chem.* **2020**, *44*, 18879−18891.

(62) Desai, R.; Mehta, R. V.; Upadhyay, R. V.; Gupta, A.; Praneet, A.; Rao, K. V. Bulk magnetic properties of CdFe2O4 in nano-regime. *Bull. Mater. Sci.* **2007**, *30*, 197−203.

(63) Joshi, H. M.; Lin, Y. P.; Aslam, M.; Prasad, P. V.; Schultz-Sikma, E. A.; Edelman, R.; Meade, T.; Dravid, V. P. Effects of shape and size of cobalt ferrite nanostructures on their MRI contrast and thermal activation. *J. Phys. Chem. C* **2009**, *113*, 17761−17767.

(64) Bhagwat, V. R.; Humbe, A. V.; More, S. D.; Jadhav, K. M. Sol-gel auto combustion synthesis and characterizations of cobalt ferrite nanoparticles: Different fuels approach. *Mater. Sci. Eng., B* **2019**, *248*, 114388.

(65) Lu, A.-H.; Salabas, E. L.; Schüth, F. Magnetic nanoparticles: synthesis, protection, functionalization, and application. *Angew. Chem., Int. Ed.* **2007**, *46*, 1222−1244.

(66) Houshiar, M.; Zebhi, F.; Razi, Z. J.; Alidoust, A.; Askari, Z. Synthesis of cobalt ferrite (CoFe2O4) nanoparticles using combustion, coprecipitation, and precipitation methods: A comparison study of size, structural, and magnetic properties. *J. Magn. Magn. Mater.* **2014**, *371*, 43−48.

(67) Sharma, N. D.; Verma, M. K.; Choudhary, N.; Sharma, S.; Singh, D. Enhanced coercivity of NiFe$_{1−x}$Dy$_x$CrO$_4$ ferrites synthesized by glycine-nitrate combustion method. *Mater. Sci. Technol.* **2019**, *35*, 448−455.

(68) Stoner, E. C.; Wohlfarth, E. P. A mechanism of magnetic hysteresis in heterogeneous alloys. *Philos. Trans. R. Soc., A* **1948**, *240*, 599−642.

(69) Choudhary, N.; Verma, M. K.; Sharma, N. D.; Sharma, S.; Singh, D. Superparamagnetic nanosized perovskite oxide La$_{0.5}$Sr$_{0.5}$Ti$_{0.5}$Fe$_{0.5}$O$_3$ synthesized by modified polymeric precursor method: effect of calcination temperature on structural and magnetic properties. *J. Sol. Gel Sci. Technol.* **2018**, *86*, 73−82.

(70) Praveena, K.; Sadhana, K.; Virk, H. S. Structural and magnetic properties of Mn-Zn ferrites synthesized by microwave-hydrothermal process. *Solid State Phenom.* **2015**, *232*, 45−64.

(71) Sijo, A. K.; Jha, V. K.; Kaykan, L. S.; Dutta, D. P. Structure and cation distribution in superparamagnetic NiCrFeO$_4$ nanoparticles using Mössbauer study. *J. Magn. Magn. Mater.* **2020**, *497*, 166047.

(72) Goyal, A.; Kapoor, S.; Samuel, P.; Kumar, V.; Singhal, S. Facile protocol for reduction of nitroarenes using magnetically recoverable CoM$_{0.2}$Fe$_{1.8}$O$_4$ (M= Co, Ni, Cu and Zn) ferrite nanocatalysts. *RSC Adv.* **2015**, *5*, 51347−51363.

(73) Kooti, M.; Afshari, M. Magnetic cobalt ferrite nanoparticles as an efficient catalyst for oxidation of alkenes. *Sci. Iran.* **2012**, *19*, 1991−1995.

(74) Jauhar, S.; Singhal, S. Substituted cobalt nano-ferrites, CoM$_x$Fe$_{2−}$$_xO_4$ (M= Cr^{3+}, Ni^{2+}, Cu^{2+}, Zn^{2+}; 0.2≤ x≤ 1.0) as heterogeneous catalysts for modified Fenton's reaction. *Ceram. Int.* **2014**, *40*, 11845−11855.

(75) Goyal, A.; Bansal, S.; Singhal, S. Facile reduction of nitrophenols: Comparative catalytic efficiency of MFe$_2$O$_4$ (M= Ni, Cu, Zn) nano ferrites. *Int. J. Hydrogen Energy* **2014**, *39*, 4895−4908.

(76) Sharma, R. K.; Monga, Y.; Puri, A. Magnetically separable silica@ Fe$_3$O$_4$ core−shell supported nano-structured copper (II) composites as a versatile catalyst for the reduction of nitroarenes in aqueous medium at room temperature. *J. Mol. Catal. A: Chem.* **2014**, *393*, 84−95.

(77) Chen, X.; Wang, W.; Xiao, H.; Hong, C.; Zhu, F.; Yao, Y.; Xue, Z. Accelerated TiO$_2$ photocatalytic degradation of Acid Orange 7 under visible light mediated by peroxymonosulfate. *Chem. Eng. J.* **2012**, *193−194*, 290−295.

(78) Anipsitakis, G. P.; Dionysiou, D. D. Radical generation by the interaction of transition metals withcommon oxidants. *Environ. Sci. Technol.* **2004**, *38*, 3705−3712.

(79) Kostedt, W. L.; Drwiega, J.; Mazyck, D. W.; Lee, S.-W.; Sigmund, W.; Wu, C.-Y.; Chadik, P. Magnetically agitated photo-catalytic reactor for photocatalytic oxidation of aqueous phase organic pollutants. *Environ. Sci. Technol.* **2005**, *39*, 8052−8056.

(80) Gupta, N. K.; Ghaffari, Y.; Kim, S.; Bae, J.; Kim, K. S.; Saifuddin, M. Photocatalytic degradation of organic pollutants over MFe$_2$O$_4$ (M= Co, Ni, Cu, Zn) nanoparticles at neutral Ph. *Sci. Rep.* **2020**, *10*, 4942.

(81) Fardood, S. T.; Atrak, K.; Ramazani, A. Green synthesis using tragacanth gum and characterization of Ni−Cu−Zn ferrite nano-particles as a magnetically separable photocatalyst for organic dyes degradation from aqueous solution under visible light. *J. Mater. Sci. Mater. Electron.* **2017**, *28*, 10739−10746.

(82) Mai, F. D.; Chen, C. C.; Chen, J. L.; Liu, S. C. Photodegradation of methyl green using visible irradiation in ZnO suspensions. *J. Chromatogr. A* **2008**, *1189*, 355−365.

(83) Habibi, M. H.; Talebian, N.; Choi, J.-H. The effect of annealing on photocatalytic properties of nanostructured titanium dioxide thin films. *Dyes Pigm.* **2007**, *73*, 103−110.

(84) Parvizi, E.; Tayebee, R.; Koushki, E.; Abdizadeh, M. F.; Maleki, B.; Audebert, P.; Galmiche, L. Photocatalytic efficacy of supported tetrazine on MgZnO nanoparticles for the heterogeneous photo-degradation of methylene blue and ciprofloxacin. *RSC Adv.* **2019**, *9*, 23818−23831.

(85) Xie, T.; Xu, L.; Liu, C.; Wang, Y. Magnetic composite ZnFe$_2$O$_4$/SrFe$_{12}$O$_{19}$: Preparation, characterization, and photocatalytic activity under visible light. *Appl. Surf. Sci.* **2013**, *273*, 684−691.

(86) Gao, Y.; Gan, H.; Zhang, G.; Guo, Y. Visible light assisted Fenton-like degradation of rhodamine B and 4-nitrophenol solutions with a stable poly-hydroxyl-iron/sepiolite catalyst. *Chem. Eng. J.* **2013**, *217*, 221−230.

(87) Magalhães, F.; Pereira, M. C.; Botrel, S. E. C.; Fabris, J. D.; Macedo, W. A.; Mendonça, R.; Lago, R. M.; Oliveira, L. C. A. Cr-containing magnetites Fe$_{3−x}$Cr$_x$O$_4$: the role of Cr^{3+} and Fe^{2+} on the stability and reactivity towards H$_2$O$_2$ reactions. *Appl. Catal., A* **2007**, *332*, 115−123.

(88) Zhang, D.; Wang, Q.; Wang, L.; Zhang, L. Magnetically separable CdFe$_2$O$_4$/graphene catalyst and its enhanced photocatalytic properties. *J. Mater. Chem. A* **2015**, *3*, 3576−3585.

(89) Zhang, W.; Wang, M.; Zhao, W.; Wang, B. Magnetic composite photocatalyst ZnFe$_2$O$_4$/BiVO$_4$: synthesis, characterization, and visible-light photocatalytic activity. *Dalton Trans.* **2013**, *42*, 15464−15474.

(90) Reddy, K. H.; Martha, S.; Parida, K. M. Fabrication of novel p-BiOI/n-ZnTiO$_3$ heterojunction for degradation of rhodamine 6G under visible light irradiation. *Inorg. Chem.* **2013**, *52*, 6390−6401.

(91) Nashim, A.; Martha, S.; Parida, K. M. Gd$_2$Ti$_2$O$_7$/In$_2$O$_3$: Efficient Visible-Light-Driven Heterojunction-Based Composite Photocatalysts for Hydrogen Production. *ChemCatChem* **2013**, *5*, 2352−2359.

(92) Bhirud, A.; Sathaye, S.; Waichal, R.; Park, C.-J.; Kale, B. In situ preparation of N-ZnO/graphene nanocomposites: excellent candidate as a photocatalyst for enhanced solar hydrogen generation and high-performance supercapacitor electrode. *J. Mater. Chem. A* **2015**, *3*, 17050−17063.

(93) Yu, J.; Dai, G.; Xiang, Q.; Jaroniec, M. Fabrication and enhanced visible-light photocatalytic activity of carbon self-doped TiO$_2$ sheets with exposed {001} facets. *J. Mater. Chem.* **2011**, *21*, 1049−1057.

(94) Xu, Q. C.; Wellia, D. V.; Ng, Y. H.; Amal, R.; Tan, T. T. Y. Synthesis of porous and visible-light absorbing Bi$_2$WO$_6$/TiO$_2$ heterojunction films with improved photoelectrochemical and photocatalytic performances. *J. Phys. Chem. C* **2011**, *115*, 7419−7428.

(95) Sharma, R.; Bansal, S.; Singhal, S. Tailoring the photo-Fenton activity of spinel ferrites (MFe$_2$O$_4$) by incorporating different cations (M= Cu, Zn, Ni and Co) in the structure. *RSC Adv.* **2015**, *5*, 6006−6018.

(96) Dhiman, M.; Tripathi, M.; Singhal, S. Structural, optical and photocatalytic properties of different metal ions (Cr^{3+}, Co^{2+}, Ni^{2+}, Cu^{2+} and Zn^{2+}) substituted quaternary perovskites. *Mater. Chem. Phys.* **2017**, *202*, 40−49.

(97) Chang, C.-W.; Hu, C. Graphene oxide-derived carbon-doped SrTiO$_3$ for highly efficient photocatalytic degradation of organic pollutants under visible light irradiation. *Chem. Eng. J.* **2020**, *383*, 123116.

(98) Kapoor, S.; Goyal, A.; Bansal, S.; Singhal, S. Emergence of bismuth substituted cobalt ferrite nanostructures as versatile candidates for the enhanced oxidative degradation of hazardous organic dyes. *New J. Chem.* **2018**, *42*, 14965−14977.